Bulletin of the Seismological Society of America, Vol. 104, No. 1, pp. 73–94, February 2014, doi: 10.1785/0120130106

Spectral-Element Simulations of Seismic Waves Generated by the 2009 L'Aquila Earthquake

by Federica Magnoni, Emanuele Casarotti, Alberto Michelini, Antonio Piersanti, Dimitri Komatitsch, Daniel Peter, and Jeroen Tromp

Abstract We adopt a spectral-element method (SEM) to perform numerical simulations of the complex wavefield generated by the 6 April 2009 M_w 6.3 L'Aquila earthquake in central Italy. The mainshock is represented by a finite-fault solution obtained by inverting strong-motion and Global Positioning System data, testing both 1D and 3D wavespeed models for central Italy. Surface topography, attenuation, and the Moho discontinuity are also accommodated. Including these complexities is essential to accurately simulate seismic-wave propagation. Three-component synthetic waveforms are compared to corresponding velocimeter and strong-motion recordings. The results show a favorable match between data and synthetics up to ~0.5 Hz in a 200 km × 200 km × 60 km model volume, capturing features mainly related to topography or low-wavespeed basins. We construct synthetic peak ground velocity maps that, for the 3D model, are in good agreement with observations, thus providing valuable information for seismic-hazard assessment. Exploiting the SEM in combination with an adjoint method, we calculate finite-frequency kernels for specific seismic arrivals. These kernels capture the volumetric sensitivity associated with the selected waveform and highlight prominent effects of topography on seismic-wave propagation in central Italy.

Online Material: Movie of wave propagation, waveform fits, and stable of station parameters.

Introduction

The 6 April 2009 M_w 6.3 L'Aquila earthquake had a severe impact on the Abruzzi region in terms of destruction and casualties. Imaging of the source (Anzidei *et al.*, 2009; Atzori *et al.*, 2009; Cirella *et al.*, 2009, 2012; Pino and Di Luccio, 2009; Cheloni *et al.*, 2010; Scognamiglio *et al.*, 2010) highlights a complex rupture history composed of two main slip releases and controlled by spatial variations of material properties along the fault (Chiarabba *et al.*, 2010; Lucente *et al.*, 2010; Di Stefano, Chiarabba, *et al.*, 2011) as well as temporal variations (Lucente *et al.*, 2010; Zaccarelli *et al.*, 2011). The source characteristics are partly responsible for the southeast directivity (Pino and Di Luccio, 2009; Akinci *et al.*, 2010) and the unusually high levels of strong acceleration recorded close to L'Aquila city (Ameri *et al.*, 2009; Çelebi *et al.*, 2010). We note that all previous source imaging studies have adopted 1D layered seismic wavespeed models for the inversion, even excluding the topography which, however, is relevant in a region like Abruzzo that is crossed by the Apennines. Volpe *et al.* (2012) performed a linear inversion of geodetic deformation data for the main event that includes a 3D tomographic model and surface topography. They show that adopting a realistic 3D structural model has considerable impact on the retrieved source parameters, because homogeneous or 1D layered models can introduce trade-offs between structural and source parameters. Utilizing complex structural models for high-resolution simulations of seismic-wave propagation is challenging, especially if a realistic finite source is also accounted for. Needless to say, accurate simulations are critical for quantitative seismic-hazard assessment.

In this article, we seek to compare observed and simulated seismic waveforms for the 2009 L'Aquila earthquake. We take into account existing knowledge of 3D features of the region, namely significant topography and complex geology. To accommodate topography, we adopt Shuttle Radar Topographic Mission (SRTM) data (Jarvis *et al.*, 2008), and for the 3D structural model we use the tomographic model of Chiarabba *et al.* (2010) for central Italy. Finally, we adopt the finite-source solution proposed by Cirella *et al.* (2009), which was obtained based on a nonlinear joint inversion of accelerometer and Global Positioning System (GPS) records.

In order to accurately simulate complete waveforms for complex media and events, suitable numerical methods are required. Several research groups worldwide are using the most advanced 3D numerical techniques and tools for both forward and inverse modeling. The finite-difference method is probably the most widely used (e.g., Madariaga, 1976; Virieux, 1986; Olsen and Archuleta, 1996; Moczo *et al.*, 2007), but in that technique it is difficult to accurately handle sharp topographic variations and their effect on seismic-wave propagation (see for instance Tarras *et al.*, 2011, and references therein). Thus, for regions such as central Italy in which topography is significant we prefer to resort to a finite-element technique, in which handling topography is natural and accurate. Other methods include spectral and pseudospectral techniques (e.g., Carcione, 1994), which are characterized by high accuracy, or finite-element methods (FEMs), which have been successfully used for seismic-wave simulations in 3D sedimentary basins because of their geometrical flexibility (e.g., Bao *et al.*, 1998). The ADER-DG method (e.g., Arnold, 1982; Falk and Richter, 1999; Hu *et al.*, 1999; Rivière and Wheeler, 2003; Monk and Richter, 2005; Käser and Dumbser, 2006) exploits the geometrical advantages offered by tetrahedral meshes and thus appears promising because of improved flexibility in the mesh creation step when compared to other high-order methods, while preserving comparable accuracy. However, from a computational perspective it is significantly more expensive. In this article, we adopt the spectral-element method (SEM), which combines the accuracy of pseudospectral methods with the flexibility of the FEM, thereby providing key advantages in terms of computational performance (e.g., Tromp *et al.*, 2008). If need be, the SEM can be implemented as a discontinuous Galerkin method (Kopriva *et al.*, 2002; Kopriva, 2006; Acosta Minolia and Kopriva, 2011). The SEM has been used to study 2D and 3D local, regional, and global seismic-wave propagation problems (e.g., Cohen *et al.*, 1993; Priolo *et al.*, 1994; Faccioli *et al.*, 1997; Komatitsch, 1997; Komatitsch and Vilotte, 1998; Komatitsch and Tromp, 2002a,b; Chaljub and Valette, 2004; Komatitsch *et al.*, 2004, 2005; Liu *et al.*, 2004; Stich and Morelli, 2007; Lee *et al.*, 2008; Stich *et al.*, 2009; Stupazzini *et al.*, 2009; Tape *et al.*, 2010; Zhu *et al.*, 2012a,b). In particular, in the recent work of Smerzini and Villani (2012), the SEM implemented in the code *GeoELSE* (Stupazzini *et al.*, 2009) has been used to simulate near-fault ground motions produced by the 2009 L'Aquila mainshock. The principal aim of this study was to investigate the effects of stochastically varying kinematic source descriptions on waveforms. They proposed a hybrid scheme that combines SEM synthetics for frequencies up to 2.5 Hz with higher-frequency stochastic components in order to simulate near-field ground motions over the engineering frequency range of interest.

In the following sections we present source and wavespeed models implemented in the SEM code *SPECFEM3D_Cartesian* (Peter *et al.*, 2011) for simulations of the 2009 M_w 6.3 L'Aquila earthquake. Comparisons between observed data and SEM synthetics produced for flat versus undulating models emphasize the importance of topography for realistic ground-motion simulations. Furthermore, comparisons between data and synthetics for 1D and 3D wavespeed models of the region clearly demonstrate the importance of 3D models for accurate ground-motion simulations. Valuable implications for seismic-hazard analyses can be deduced from synthetic peak ground velocity (PGV) maps obtained using *SPECFEM3D_Cartesian* and a fully 3D model for central Italy. Finally, by exploiting the adjoint approach (e.g., Tarantola, 1984; Akçelik *et al.*, 2003; Tromp *et al.*, 2005, 2008; Fichtner, 2010), we determine 3D finite-frequency sensitivity kernels to illuminate those structural features responsible for specific phases observed in seismograms (e.g., Tape *et al.*, 2010).

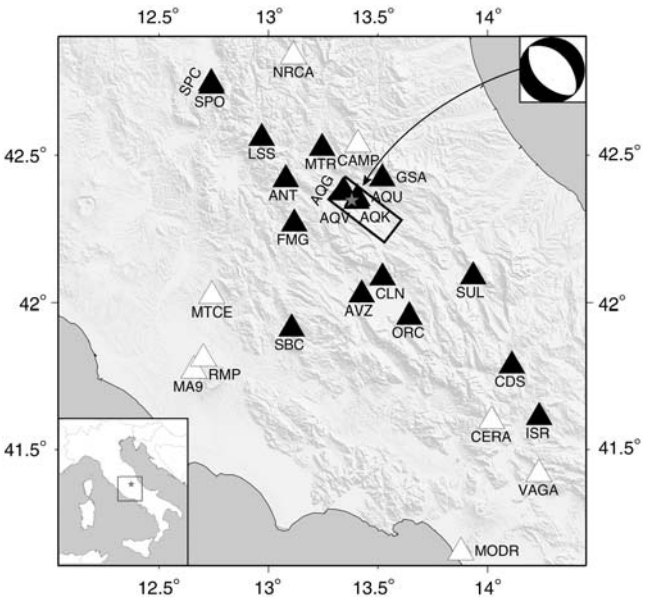

Figure 1. The study area in central Italy, with dimensions of 200 km × 200 km used for SEM simulations of the wavefield generated by the 2009 M_w 6.3 L'Aquila event. The gray star represents the location of the mainshock; the focal mechanism was obtained by the Time Domain Moment Tensor (TDMT) solution (see Data and Resources); and the black rectangle indicates the fault plane. Triangles represent 26 stations used in this study: white triangles, the eight velocimeters of the Italian National Seismic Network (INSN); black triangles, 18 accelerometers (17 of the Italian strong-motion network [RAN] and 1 placed at the Mediterranean Very Broadband Seismographic Network [MedNet] station AQU).

The 2009 L'Aquila Earthquake

On 6 April 2009 at 01:32 UTC the Abruzzi region was struck by an earthquake with moment magnitude M_w 6.3 at centroid location 42.35° N, 13.38° E at a depth of 9.5 km (e.g., Chiaraluce, 2012). Rupture occurred on a normal fault striking northwest–southeast along the central Apennines axis and dipping at about 50° to the southwest (Fig. 1). The event caused more than 300 casualties and severe damage in the city of L'Aquila and in the surrounding villages. The

mainshock was preceded by a sequence of small events that started a few months earlier. The largest foreshock occurred on 30 March 2009 with M_w 4 (e.g., Scognamiglio *et al.*, 2010). Several aftershocks followed the main event; among them, the M_w 5.6 on 7 April 2009 and the M_w 5.4 on 9 April 2009 events are the largest.

In this study, we are interested in the seismic wavefield generated by the L'Aquila mainshock. The target region (Fig. 1) features a complex tectonic structure and evolution characterized by highly variable geologic and geomorphologic patterns (e.g., Malinverno and Ryan, 1986; Patacca and Scandone, 1989; Doglioni, 1991, 1995; Scrocca, 2006). At present, the central sector of the Apennines chain involves northeast-trending horizontal extension (e.g., Mariucci *et al.*, 1999; Hunstad *et al.*, 2003; Montone *et al.*, 2004; Li *et al.*, 2007) related to the opening of the Tyrrhenian back-arc basin (e.g., Malinverno and Ryan, 1986). This extensive regime causes the formation of several intramountain basins of varying dimensions, such as the L'Aquila, Sulmona, and Fucino basins, which are covered by Plio-Quaternary continental sediments (e.g., Cavinato and De Celles, 1999; Chiarabba *et al.*, 2010; Fig. 2). Thus, most of the active faults are normal, comprising a fault system striking northwest–southeast along the Apennines and bounding the basins (e.g., Chiaraluce *et al.*, 2004; Patacca *et al.*, 2008). In particular, the epicentral area corresponds to the upper and middle Aterno valley, with Quaternary lacustrine deposits forming its basins. The depth of the deposits in this area varies from about 60 m to more than 200 m from the upper to the middle Aterno valley (Bosi and Bertini, 1970), and much evidence of ground-motion amplification has been found (e.g., De Luca *et al.*, 2005; Akinci *et al.*, 2010). Finally, remarkable topographic ridges characterize the region, including the Gran Sasso and Maiella massifs to the east and the Simbruini Mountains to the west (e.g., Chiarabba *et al.*, 2010; Fig. 2). The volume involved in our simulations extends 200 km × 200 km horizontally and 60 km in depth, with limits of latitude and longitude of 41.10°–42.90° N and 12.04°–14.45° E (Fig. 1), respectively.

For the main characteristics of the 2009 L'Aquila event we refer to the study of Cirella *et al.* (2009), who deduce the rupture history of the earthquake from a nonlinear joint inversion of seismic strong-motion and GPS data. They also provide synthetic time series that can be benchmarked against our simulations. They adopt a fault plane with a strike of N133° E and a dip of 54° to the southwest. The strike direction is taken from a Synthetic Aperture Radar interferometric data analysis (Atzori *et al.*, 2009). The dip value is consistent with both the hypocenter location and observed surface breakages (EMERGEO Working Group, 2010). In addition, the assumed strike and dip are within the range of values inferred from moment tensor solutions (see Data and Resources). The distribution of aftershocks and GPS displacements (Anzidei *et al.*, 2009) also contributed to the identification of the fault geometry. Cirella *et al.* (2009) determine a heterogeneous fault-slip distribution (see Fig. 2a therein) in which two main patches are evident, namely, a shallow small slip feature located up-dip from the hypocenter and a larger deeper feature (between 9 km and 14 km depth) located southeastward. This slip distribution is in agreement with the on-fault aftershock pattern and induced surface breakages. Moreover, they infer a larger rupture speed in the up-dip direction (~2.8 km/s) compared to the along-strike direction (~2 km/s). This is probably related to a lower wave-speed layer in the crustal profile used by Cirella *et al.* (2009) at depths corresponding to the largest slip patch, suggesting strong structural control of the rupture process (Cirella *et al.*, 2012).

Data

The 2009 M_w 6.3 L'Aquila mainshock was recorded by a dense network of receivers (e.g., Akinci *et al.*, 2010; Chiarabba *et al.*, 2010). Among the available records we rejected those that showed clipped signals. The final dataset consists of eight velocimetric stations of the Italian National Seismic Network (INSN), managed by the Istituto Nazionale di Geofisica e Vulcanologia (INGV), and 17 accelerometric stations of the Italian strong-motion network (RAN), managed by the Italian Civil Protection agency. In addition, AQU, a very broadband station of the Mediterranean Very Broadband Seismographic Network (MedNet) operated by INGV, was equipped with an accelerometer. The locations of the 26 receivers are shown in Figure 1.

Inclusion of accelerometric records is very useful when dealing with moderate to large earthquakes, such as the L'Aquila mainshock. In fact, these time series provide on-scale seismic signals recorded very close to the event, and, in other studies, they have been used to estimate, for example, source parameters, seismic attenuation, and local site amplification effects (e.g., Bindi *et al.*, 2009; Cirella *et al.*, 2009; Akinci *et al.*, 2010).

It is worth noting that 13 out of the 26 stations included here were used in the source inversion of Cirella *et al.* (2009). Specifically, they are the 12 accelerometers of the RAN and the accelerometer collocated at the AQU MedNet station. A preliminary comparison between the synthetics calculated by Cirella *et al.* (2009) and those simulated using *SPECFEM3D_Cartesian*, adopting the same source and structural models, showed reasonable agreement between the simulated waveforms (Magnoni, 2012). Overall, this test demonstrated that the source model parametrization adopted in our simulations is consistent with the results obtained by Cirella *et al.* (2009).

For proper comparisons, recorded seismograms and synthetic waveforms calculated using *SPECFEM3D_Cartesian* underwent the same processing steps. In particular, accelerometric data and SEM acceleration synthetics were integrated to obtain ground velocities, and band-pass filtered with corner frequencies of 0.02 Hz and 0.5 Hz. Synthetics for the velocimetric stations were convolved with the appropriate instrument response and subsequently filtered between

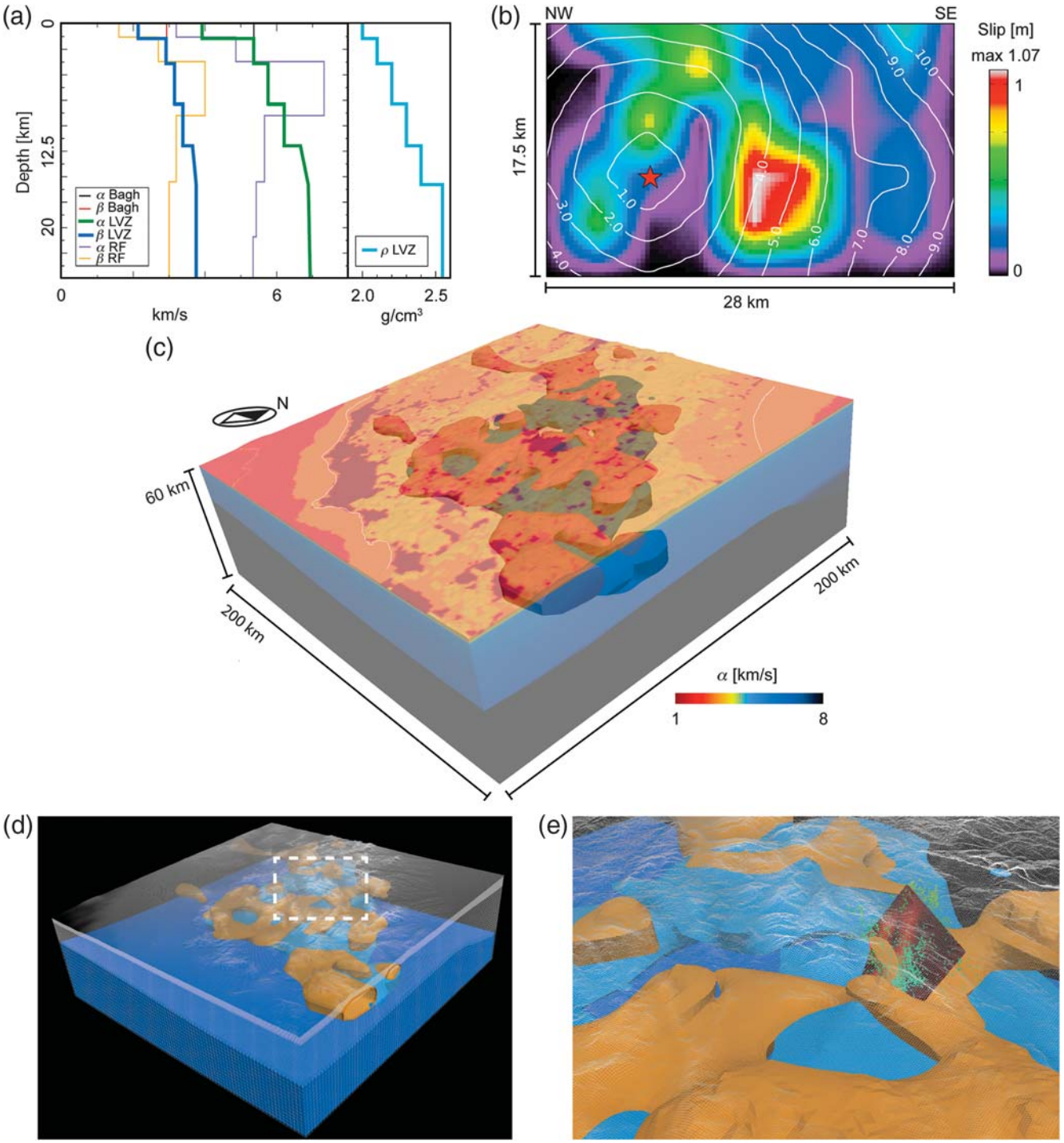

Figure 2. (a) 1D wavespeed and density profiles for the central-Italy region, courtesy of Cirella *et al.* (2009). Models m1DF and m1DT include vertical profiles (LVZ) that are based upon the crustal model of Bagh *et al.* (2007; labeled Bagh), modified with a shallow (0–1.5 km) low-wavespeed layer from Herrmann and Malagnini (2009). Profiles labeled RF are derived from receiver function studies at specific stations, but we do not include this information in our models. Density values ρ (in g/cm^3) are shown on the right. (b) On-fault slip distribution for the 2009 M_w 6.3 L'Aquila earthquake. It was obtained by discretizing the finite source of the mainshock into 7063 point sources and by interpolating the source parameters determined by Cirella *et al.* (2009); the rupture time is shown by white contour lines (in seconds). The red star indicates the mainshock hypocenter. (c) View from the southeast of the 3D wavespeed model (m3D) in central Italy. The scale for α is on the bottom right; β is calculated from α and α/β. The model volume is 200 km × 200 km × 60 km, and the homogeneous layer below the Moho surface (Di Stefano and Bianchi *et al.*, 2011) is denoted in black. In transparency, the internal tomographic model is shown. Blue features correspond to $\alpha = 6.4$ km/s, orange features correspond to $\alpha/\beta = 1.84$. (d) View from the southeast of the hexahedral mesh used to implement model m3D into *SPECFEM3D_Cartesian*. The element size increases from the top to the bottom by means of two mesh triplings. The spatial scale, as well as blue and orange features, are the same as in (c). (e) Close up of the white inset in (d). The fault plane of the 2009 L'Aquila event is shown, together with aftershocks that occurred in the 10 days following the mainshock (green squares).

0.02 Hz and 0.5 Hz, like the corresponding observed velocities.

Numerical Method

The accuracy of the SEM in simulating complex events at local scales, combined with its computational efficiency and ease of use, make it a very good option for our purposes. The SEM is based on a weak formulation of the seismic-wave equation that guarantees very accurate modeling of surface waves (e.g., Komatitsch *et al.*, 2005). Moreover, the method uses high-order Lagrange polynomials to interpolate the wavefield, together with Gauss–Lobatto–Legendre (GLL) quadrature, both defined on the same GLL points, thus leading to a perfectly diagonal mass matrix. Therefore, it is possible to adopt an explicit time scheme to integrate the global system, thereby accommodating a very efficient implementation on parallel computers (e.g., Tromp *et al.*, 2008; Komatitsch, 2011; Peter *et al.*, 2011). In addition, the high-degree Lagrange polynomials assure exponential spatial accuracy. Thorough reviews of the SEM in seismology can be found, e.g., in Komatitsch *et al.* (2005), Chaljub *et al.* (2007), Tromp *et al.* (2008), and Fichtner (2010).

In this article, we use the spectral-element software package *SPECFEM3D_Cartesian* (i.e., the version of *SPECFEM3D* for local/regional simulations, see Data and Resources; Peter *et al.*, 2011) for forward simulations of the wavefield generated by the 2009 L'Aquila event. This software package allows us to accommodate all complexities that affect seismic-wave propagation, such as topography, lateral wavespeed variations, attenuation, anisotropy, absorbing conditions at model boundaries as well as a finite-source description. In particular, we use a kinematic source model, although the code also allows for dynamic rupture modeling (e.g., Madariaga *et al.*, 2006; Huang *et al.*, 2013). The input elements for the code are models of the wavespeed structure and of the seismic source. The model volume is discretized using a mesh of hexahedral elements, and the values of the material properties are assigned to each GLL point. These aspects will be discussed in more details in the following sections.

Using *SPECFEM3D_Cartesian*, we simulate 60 s long three-component seismograms at all 26 stations in a volume of 200 km × 200 km × 60 km. The kinematic source was determined by Cirella *et al.* (2009), and both 1D models (with and without topography) and 3D wavespeed models are tested, using appropriate meshes. High-performance computational facilities at INGV were used for the simulations, running parallel jobs on the cluster ELIOS, which has 64 compute nodes, each with 2 quad-core AMD Opteron 2374 processors at 2.4 GHz and with 16 GB of RAM (512 total cores, 2 GB of RAM/core). Using the 3D wavespeed model, a forward simulation of 60 s duration requires 32 hr on 308 cores. In this article, we also use the same SEM code in combination with an adjoint method to construct finite-frequency sensitivity kernels defined by specific phases in observed seismograms.

Geological Model and Mesh

Central Italy has a very intriguing and complicated internal structure that is characterized by a complex Moho and a highly heterogeneous impedance profile with numerous shallow and poorly constrained sedimentary basins. Among the largest are the Piana del Fucino and Aterno basins, which are immediately adjacent to the fault associated with the 2009 M_w 6.3 L'Aquila mainshock. Numerous other small Apennines basins are poorly constrained, especially vertically. Nevertheless, they play a key role in the description of site effects that are prominent in this region (e.g., Bindi *et al.*, 2004, 2009; Castro *et al.*, 2004). We considered the 3D tomographic model of Chiarabba *et al.* (2010) and included the V_{S30} layer of Michelini *et al.* (2008) to account for basin amplification. The resulting model, hereafter labeled the m3D model, covers a region of 200 km × 200 km × 60 km in central Italy. The material properties of the structure below the Moho are taken from Di Stefano and Bianchi *et al.* (2011). A description of the main features of the geology is inserted in Figure 2c.

In order to take full advantage of the capabilities of the SEM, *SPECFEM3D_Cartesian* requires that the geological volume is described by a conforming all-hexahedral unstructured mesh. The highest accuracy is obtained by honoring all structural heterogeneities, but such a detailed discretization is often impossible to achieve with hexahedral elements, requiring months of tedious art-and-craft work (e.g., Casarotti *et al.*, 2008). Moreover, uncertainties in the 3D tomographic model do not warrant such a detailed mesh. Thus, we exploit the option of letting the seismological parameters (wavespeeds, density, and attenuation) vary inside each element and, by so doing, the tomographic model is replicated through interpolation. The resulting mesh, shown in Figure 2d–e, covers the entire model volume and honors the Moho surface as described by Di Stefano and Bianchi *et al.* (2011) and a 90 m resolution SRTM topography. It has been constructed using *GEOCUBIT* (Casarotti *et al.*, 2008), a collection of Python scripts that provides parallel access to the meshing tools offered by the *CUBIT* mesh generation package (see Data and Resources) that is explicitly designed for geological applications. The mesh is unstructured and composed of about 7.6 million hexahedral elements. The resolution on the surface is 200 m and it decreases by means of 2 refining mesh layers to 1800 m below the Moho. This mesh has been designed for simulations that are numerically accurate up to ~5 Hz (i.e., significantly beyond the expected accuracy of our structural and source models) to be completely sure of the accuracy of our numerical simulations. The adoption of a parallel hexahedral mesher facilitates unstructured mesh construction on 308 cores of the INGV cluster in about 20 min.

In order to benchmark our simulations in a layered model and to illustrate the effects of surface topography,

we also constructed two 1D wavespeed models for central Italy. They are based on the crustal profile used by Cirella *et al.* (2009), which combines the 1D model of Bagh *et al.* (2007) with a shallow low wavespeed layer from Herrmann and Malagnini (2009), shown in Figure 2a. One of the two models also includes topography from the SRTM data. In order to run the simulations, the 1D profiles are implemented in a simple homogeneous hexahedral mesh, with 259,200 elements of size 1 km^3 and with a resolution of about 0.5 Hz. Hereafter, the 1D models with and without topography are labeled m1DT and m1DF, respectively.

Both the m3D and m1DT models account for seismic-wave attenuation by calculating the quality factor, Q, via $Q = 0.02\beta$, in which β denotes the shear wavespeed, a relationship also adopted by Olsen *et al.* (2003) and consistent with studies on attenuation in central Italy (e.g., Castro *et al.*, 2004 and Bindi *et al.*, 2009 and references therein). Mass density, ρ, is estimated via a quadratic function of compressional wavespeed, α, using the relationship $\rho = 0.025\alpha^2 - 0.055\alpha + 2.134$ (in which ρ is in g/cm^3 and α in km/s), empirically determined by interpolating gravity data and geological models (Di Luzio *et al.*, 2009; see figs. 7 and 8 therein).

Finite-Source Model

Our representation of the 2009 L'Aquila main event is based on the kinematic source model of Cirella *et al.* (2009) that incorporates both geodetic and seismological data in the inversion procedure. Relying on their model, the fault plane is 28 km long and 17.5 km wide, as shown in Fig. 2b, and the strike and dip angles are fixed at N133° E and 54° to the southwest, respectively.

Cirella *et al.* (2009) subdivide the finite fault into subpatches and assign model parameters, peak slip speed, slip direction, rupture time, and rise time, to the patch corners, with a final resolution of ~258 m and a maximum resolvable frequency of ~0.5 Hz. The model parameters are allowed to vary within each subpatch through bilinear interpolation of the nodal values. They adopt a single window approach and the source-time function is represented by a regularized Yoffe function (Tinti *et al.*, 2005) with time to peak slip velocity equal to 0.225 s. Their joint inversion of strong motion and static displacement records is performed using a two-stage nonlinear technique (Piatanesi *et al.*, 2007). During the first stage a heat-bath simulated-annealing algorithm constructs the ensemble of models that efficiently sample the good data-fitting regions. For the forward modeling they use a discrete wavenumber technique (Spudich and Xu, 2003) with 1D Green's functions. A combined cost function for seismological and geodetic data quantifies the goodness of a model. In the second stage the algorithm performs a statistical analysis of the model ensemble, which results in an average stable model of the earthquake rupture parameters in agreement with the data, from which the final slip distribution is derived (see fig. 2a in Cirella *et al.*, 2009).

Using our code, a finite fault must be discretized into point sources, described by the moment density tensor components, location, rupture time, and half duration. In order to reproduce the same fault extent as in Cirella *et al.* (2009), we construct a grid with points located at the center of each patch and again with a resolution of 258 m. This results in a finite fault discretized with 7063 point sources, each of which has source parameters obtained by interpolating those of Cirella *et al.* (2009). Thus, the on-fault slip, rise time, and rupture time distributions agree very well with those obtained by Cirella *et al.* (2009; Fig. 2b). Moreover, given the resolution and rise time history of this finite fault, the frequency content is limited to ~0.5 Hz, as expected. The moment density tensor components of each subsource are calculated by estimating the shear modulus from the values of shear wavespeed and density of the appropriate structural model (m1DF, m1DT, or m3D).

Simulations with 1D Models: Topographic Effects

Several studies document the importance of including realistic descriptions of surface topography to accurately reproduce seismic-wave propagation and surface ground motion (e.g., Kawase and Aki, 1990; Bouchon and Barker, 1996; Bouchon *et al.*, 1996; Spudich *et al.*, 1996; Komatitsch and Vilotte, 1998; Komatitsch *et al.*, 2004; Lee *et al.*, 2008; Lee, Chan, *et al.*, 2009; Lee, Komatitsch, *et al.*, 2009; Monteiller *et al.*, 2013). In addition, these studies highlight the ability of the SEM to accommodate such complexity in simulations at very high resolution (e.g., Lee, Chan, *et al.*, 2009). In general, surface topography can cause complex wave propagation phenomena, with seismic energy reflected and scattered by mountain ridges (as shown by several studies, e.g., Massa *et al.*, 2010, and references therein; Monteiller *et al.*, 2013). In particular, ground motions amplify on hilltops and along ridges (e.g., Çelebi, 1987; Kawase and Aki, 1990; Bouchon and Barker, 1996; Bouchon *et al.*, 1996; Komatitsch and Vilotte, 1998; Lee, Chan, *et al.*, 2009), with multiple reflections prolonging seismic shaking (e.g., Lee *et al.*, 2008). Remarkable variations in PGV and acceleration values have been attributed to topography, highlighting its role for seismic-hazard assessment (e.g., Komatitsch and Vilotte, 1998; Lee, Chan, *et al.*, 2009; Lee, Komatitsch, *et al.*, 2009). In central Italy, amplifications of ground motion related to topography have been observed, for example, by Marra *et al.* (2000), Donati *et al.* (2001), Marzorati *et al.* (2009), Massa *et al.* (2010), Pischiutta *et al.* (2010), and our simulation volume features relevant topographic relief. As a consequence, inclusion of topography in our models turns out to be of fundamental importance for properly simulating observed ground motions.

In this section, topographic effects on seismic waves are studied by comparing SEM synthetics calculated using models m1DF and m1DT to data. Some representative examples are shown in Figure 3. Time series are filtered between 0.02 Hz and 0.5 Hz, and all three ground-velocity components are shown. In general, considering the entire dataset

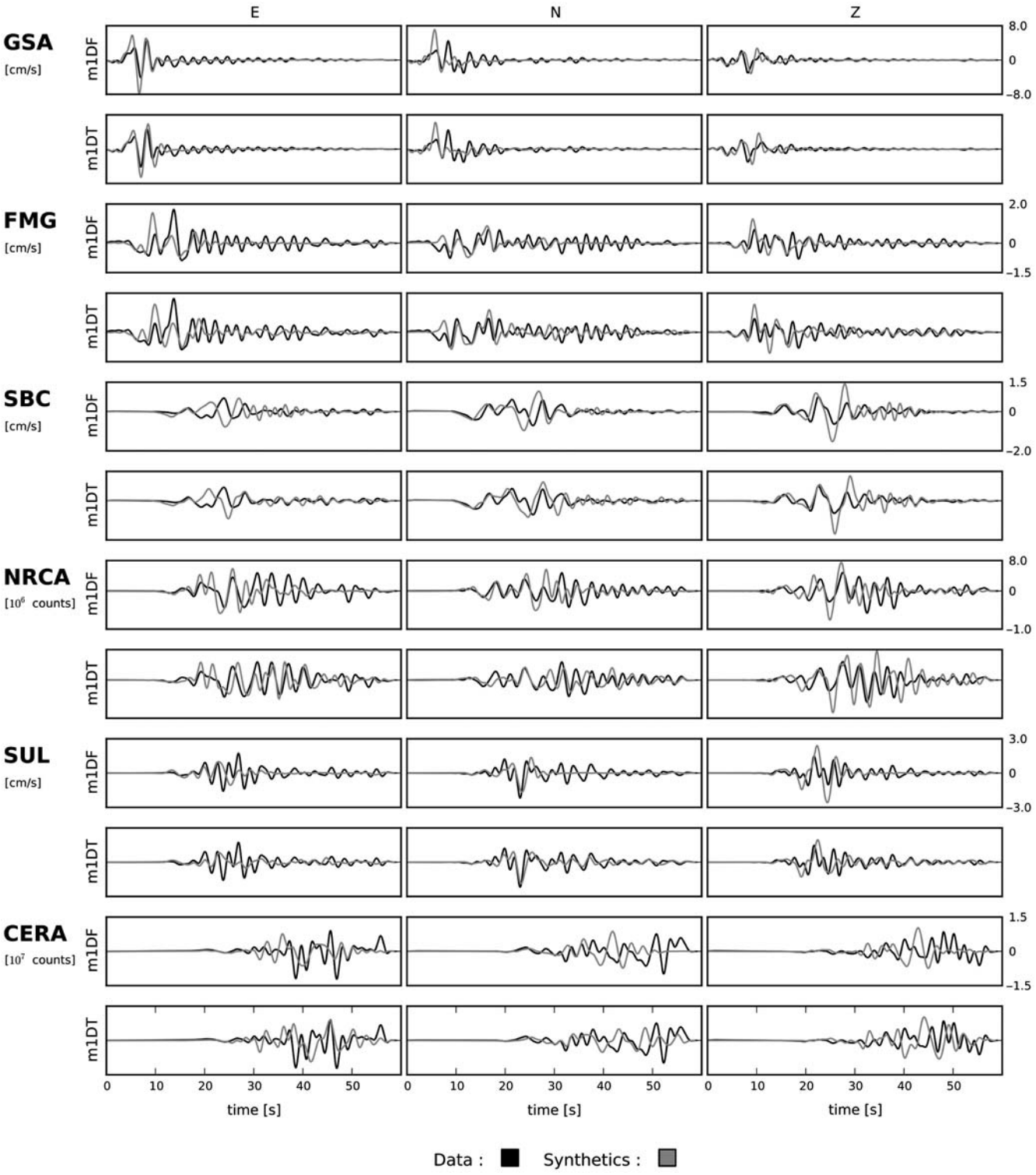

Figure 3. Three-component velocity seismograms (E, east; N, north; Z, vertical) for stations indicated by the labels on the left (see Fig. 1 for locations). The recorded time series are in black; the synthetic time series obtained by SEM simulations using the 1D wavespeed model without topography (m1DF) or the 1D model with topography (m1DT) are in gray. The seismograms are band-pass filtered in the range 0.02–0.5 Hz, and the *y* axis is the same for each station. Units are cm/s for stations GSA, FMG, SBC, and SUL and counts for stations NRCA and CERA.

(see Ⓔ Figs. S1–S7 in the electronic supplement to this article), the first part of the seismograms appears only slightly influenced by the introduction of topography, because weak variations are evident between the synthetics for the two models. This confirms that the first seconds of the waveforms are related mainly to effects of the rupture, that is, to the direct waves emitted by the source. In contrast, we see that introduction of topography in model m1DT improves the

fit between synthetics and observed seismograms in the coda part of the signal. Often, coda waves, which are related to late-arriving surface waves (e.g., Clouser and Langston, 1995; Komatitsch and Vilotte, 1998), are reproduced only by introducing topography. Hence, these features may be attributed to reflections and reverberations caused by central Apennines ridges. This is generally evident in all ground-motion components (e.g., stations SBC, SUL, and NRCA), and in some cases the fit is remarkably good (e.g., stations FMG and SUL). A quantitative analysis of topographic effects is presented in the Waveform Misfit Analysis subsection.

It is worth noting that the Cirella *et al.* (2009) source inversion is based upon a 1D flat wavespeed model, and thus topographic effects may have been partially mapped into the source model. However, Cirella *et al.* (2009) focused their analysis on the first part of the seismograms, suggesting only minor mapping of topography into source parameters. This explains why the m1DT model can be combined with the kinematic source model of Cirella *et al.* (2009).

When we analyze the results more closely, we see, however, that many features in the seismograms are still not adequately reproduced. The remaining discrepancies between data and synthetics mainly highlight the need for a 3D description of the structure, accounting for other heterogeneities in the region. This is discussed in the next section.

Finally, we note that another difference between the two 1D models considered in this section is that model m1DF does not incorporate wave attenuation. The implementation of this feature in the simulations is important, especially if the region of interest is characterized by low wavespeed sedimentary basins (e.g., Olsen *et al.*, 2003; Komatitsch *et al.*, 2004; Lee *et al.*, 2008).

Simulations with a 3D Model: Effects of Geological Structures

Modeling lateral variations in wavespeed, density, and attenuation is of paramount importance in order to accurately reproduce ground motions, as documented in many studies (e.g., Olsen *et al.*, 2003; Komatitsch *et al.*, 2004; Lee *et al.*, 2008; Chaljub, 2009; Lee, Chan, *et al.*, 2009; Lee, Komatitsch, *et al.*, 2009; Stupazzini *et al.*, 2009; Chaljub *et al.*, 2010; Tape *et al.*, 2010). In particular, areas characterized by low wavespeed sedimentary basins may show a very different ground response compared to hardrock sites, with strong amplifications, multiple reverberations, and prolonged shaking (e.g., Rovelli *et al.*, 2001; Olsen *et al.*, 2006; Chaljub *et al.*, 2007; Lee *et al.*, 2008). Moreover, these effects can be intensified and complicated by topographic ridges, which can cause amplifications, reflections, and multipathing (e.g., Lee *et al.*, 2008; Lee, Komatitsch, *et al.*, 2009). Significant site amplifications have been observed for the 2009 M_w 6.3 L'Aquila event in neighboring regions (e.g., Ameri *et al.*, 2009; Bindi *et al.*, 2009; Akinci *et al.*, 2010; Çelebi *et al.*, 2010). At L'Aquila city, for example, based on previous studies (e.g., De Luca *et al.*, 2005), these effects are related to the presence of a basin filled with lacustrine sediments with a maximum depth of 250 m. Central Italy features several other sedimentary basins, and these can have a similar influence on ground motion (e.g., Bindi *et al.*, 2004, 2009; Castro *et al.*, 2004). These effects are of primary importance for seismic-hazard assessment (e.g., Komatitsch *et al.*, 2004; Stupazzini *et al.*, 2009), strengthening our interest in modeling them in detail.

In this section, we compare SEM synthetics for model m3D to data, also highlighting differences with synthetics based on model m1DT. Figures 4–5 show comparisons for some of the stations (for the Ⓔ complete dataset, see Figs. S1–S7 in the electronic supplement to this article). The frequency range is 0.02 Hz–0.5 Hz.

We observe, as expected, that a modulation of the coda is often evident when 3D complexities are taken into account (e.g., stations AQK and AQU in Fig. 4, station MA9 in Fig. 5). Improvements in fit, both in amplitude and phase, are evident mainly on the horizontal components, where topographic effects generally are less pronounced (e.g., stations AQU and FMG in Fig. 4, station RMP in Fig. 5). On vertical components, when model m1DT already provides a good fit, model m3D often produces excessive amplification of the signal when compared to data (e.g., station FMG in Fig. 4, station SPO in Fig. 5). In many examples, these large amplitudes for the 3D model are observed on all components (e.g., stations SBC and NRCA in Fig. 4, station SPO in Fig. 5), whereas in other cases the 3D model improves the fit in both amplitude and phase (e.g., station AQK in Fig. 4, stations MA9 and RMP in Fig. 5). An interesting case is represented by station GSA (Fig. 4), where it is observed that model m3D causes strong amplification on all components between about 7.5 s and 12.5 s. This suggests that the wavespeeds are too slow along the path to this station, resulting in spurious amplification.

A more quantitative assessment of misfit is discussed in the Waveform Misfit Analysis subsection. In general, the 3D model enables us to produce (and sometime overestimate) many features in observed seismograms on all components. This confirms that 3D modeling is essential for capturing waveform complexities, that, as expected, are strongly related to lateral heterogeneities, such as sedimentary basins. These features affect mainly the horizontal components, where a good fit due to the 3D model is especially evident. Only slight changes occur in the first seconds of the traces for different structural models. This is an expected result, because this part of the seismograms is comprised of direct waves, which were exploited in the Cirella *et al.* (2009) source inversion.

Figure 6 shows the vertical component velocity wavefield simulated using *SPECFEM3D_Cartesian* and the 3D model. It illustrates clearly how wave propagation in central Italy is strongly influenced by 3D heterogeneities. Wavefront distortions are due to topographic effects and the presence of low wavespeed sedimentary basins. Ground shaking is prolonged and complicated in and around basins, where energy is trapped because of the presence of low wavespeed sediments. Waves with short wavelengths are predominantly

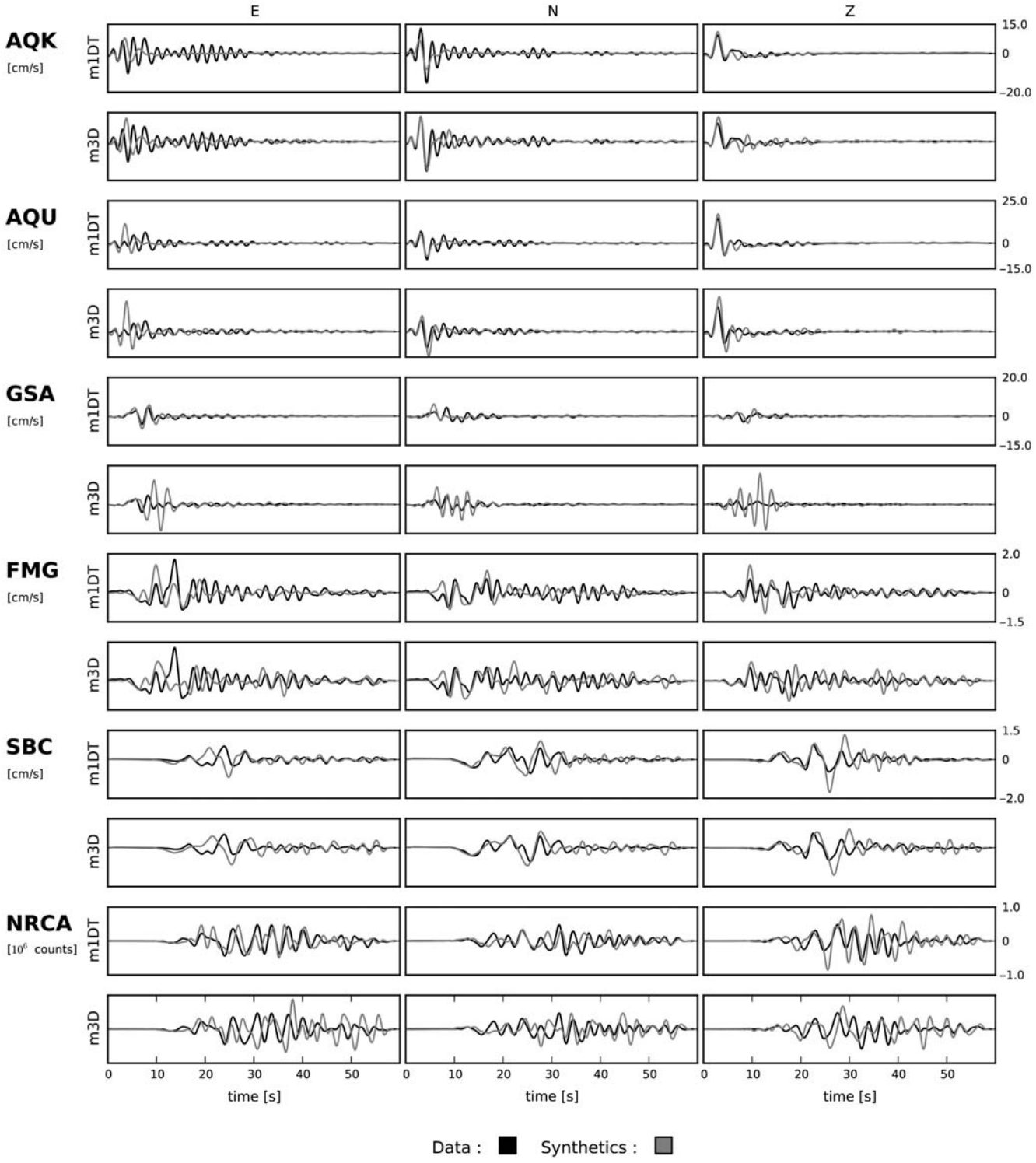

Figure 4. Three-component velocity seismograms for stations indicated by the labels on the left (see Fig. 1 for locations). The data are in black, the SEM synthetics are in gray and refer to the 1D model with topography (m1DT) or to the 3D model (m3D). The filter is 0.02–0.5 Hz, and the *y* axis is the same for each station. Units of velocity are cm/s, except for station NRCA, which is in counts.

affected by basins, suggesting that their effects become more pronounced as the frequency increases.

To conclude, we have assessed the frequency limit of our simulations by comparing data to SEM synthetics for five filtering ranges, with a maximum frequency of 1 Hz. Figure 7 shows, for one of the stations, the synthetics for model m3D (red) compared to the data (black), exemplifying common behavior for the entire dataset. Extending the frequency range, as expected, affects mainly the coda (in both observed and simulated seismograms). In the 0.02 Hz–0.5 Hz frequency

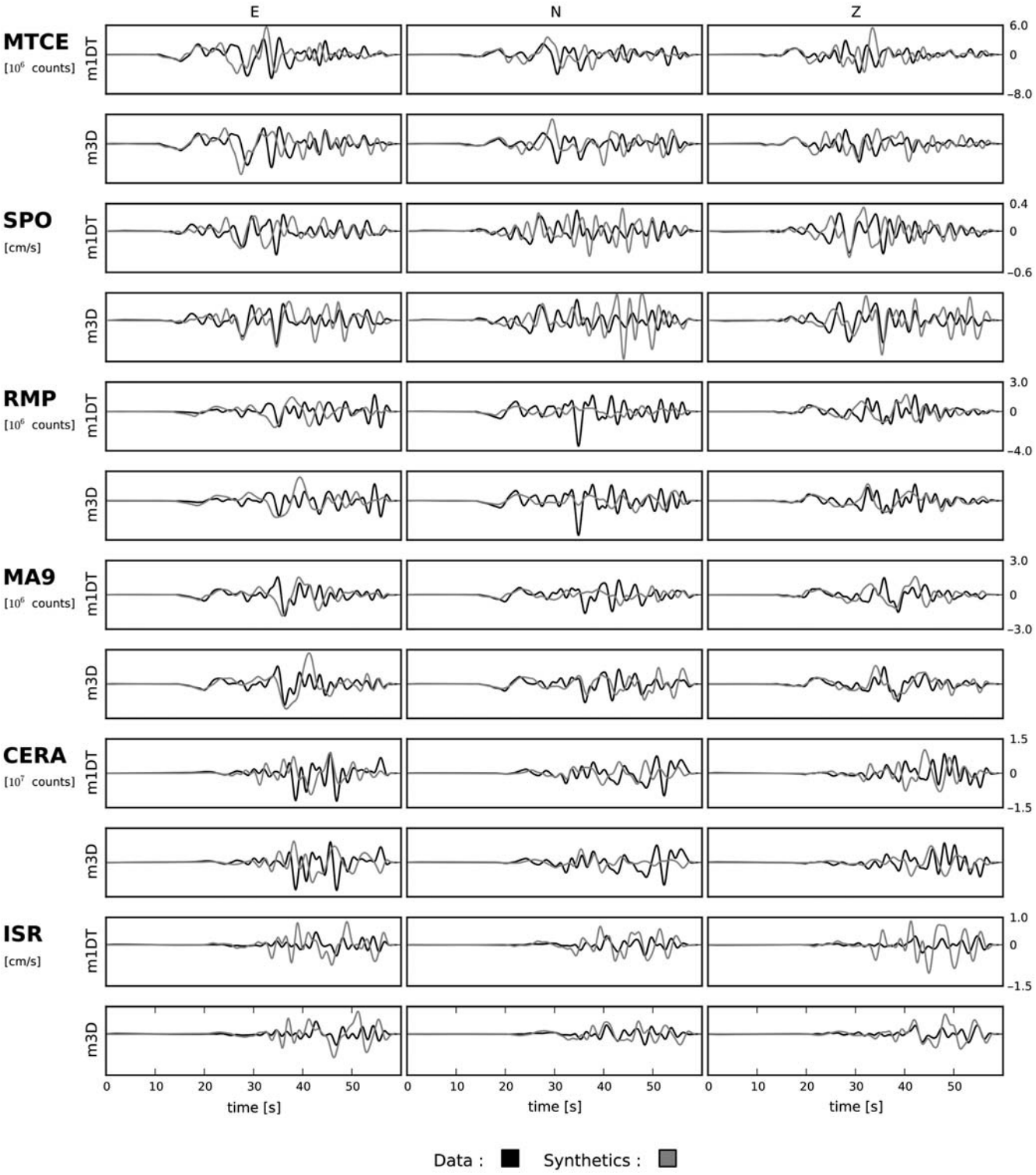

Figure 5. Same as Figure 4, showing velocity seismograms for stations SPO and ISR in cm/s; the other stations are indicated in counts.

band (which is the same as in Cirella *et al.*, 2009), multiple late arrivals become evident mostly on the horizontal components, and the corresponding 3D synthetics tend to reproduce these features. Low wavespeed sedimentary basins begin to influence waveforms in this frequency range, but the structural and source models still capture the main characteristics of the data. When the frequency range is extended up to 1 Hz, strong features in the observed seismograms become evident, which are no longer captured by the synthetics. We conclude that the structure and source models presently available for central Italy are not capable of accurately modeling seismic-wave propagation at frequencies higher than ∼0.5 Hz.

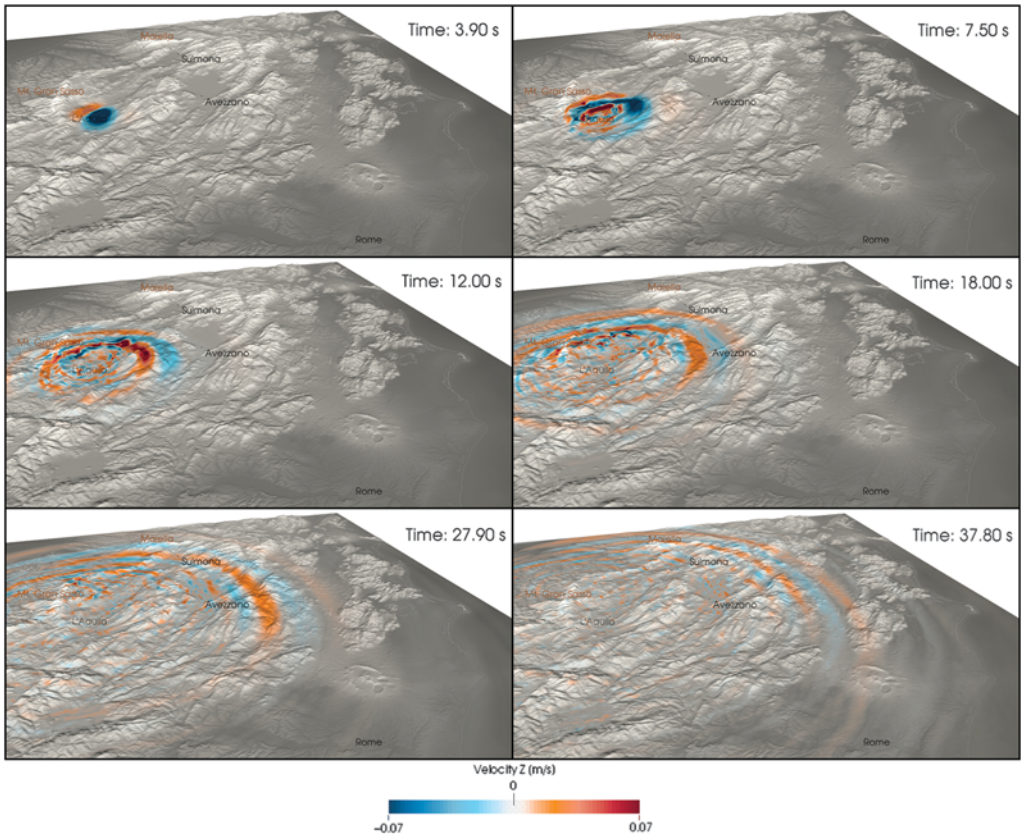

Figure 6. Snapshots at different time steps of the vertical-component velocity wavefield of the 2009 L'Aquila earthquake propagating along the surface. Red denotes positive values and blue negative values. The view is from the northwest. Wavefront distortions are due to topographic effects and to the presence of low-wavespeed sedimentary basins that trap energy and prolong ground motion.

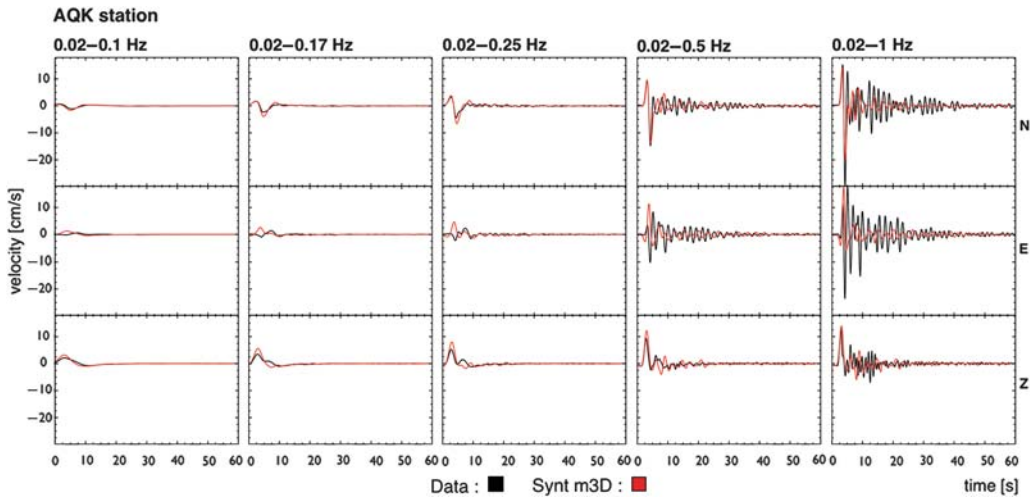

Figure 7. Three-component velocity seismogram (in cm/s) for station AQK (see map in Fig. 1) and for five frequency ranges (indicated at the top left of each column). The data are in black, and the SEM synthetics for the m3D wavespeed model are in red. The *y* axis is the same for all seismograms.

Discussion

Waveform Misfit Analysis

Visually comparing observed and simulated waveforms (Figs. 3–5) may provide some qualitative information about the effects of different structural models on simulations. However, to give more quantitative estimates of misfit between data and synthetics for a given wavespeed model, we calculate amplitude and travel-time differences within chosen time windows. The time windows are selected

manually in order to include *P*-, *S*-, and surface-wave arrivals. Using the *code measure_adj* (see Data and Resources), we calculate the cross-correlation amplitude and travel-time measurements associated with each window, namely

$$\Delta \ln A(\mathbf{m}) = \ln A^{\text{obs}} - \ln A(\mathbf{m}), \tag{1}$$

$$\Delta T(\mathbf{m}) = T^{\text{obs}} - T(\mathbf{m}), \tag{2}$$

in which A^{obs} and T^{obs} are the observed amplitude and travel time, respectively, and $A(\mathbf{m})$ and $T(\mathbf{m})$ are the corresponding predicted amplitude and travel time, respectively, for model m. In each time window, the amplitude and phase misfit is calculated by comparing data to synthetics simulated using models m1DF, m1DT, and m3D. The results are shown in Figures 8–9.

Figure 8 strongly highlights a common trend of the amplitude misfit between data and synthetics as the structural model varies from m1DF to m1DT to m3D. Using the 1D wavespeed profile without topography (see the m1DF case in Fig. 8) leads, in general, to an underestimation of observed waveform amplitudes, and this occurs primarily in their coda. The introduction of topography has a crucial effect in reducing this amplitude misfit for all components and stations, as indicated by $\Delta \ln A$ values for the m1DT case in Figure 8, which mostly tend to zero. This clearly reflects the behavior of the seismograms for model m1DT (Fig. 3), which reproduce features of observed seismograms completely missed by model m1DF. The free surface with its topography is the only first-order discontinuity for which we know the exact geometry, and by itself it contains essential information to model primary features of ground-motion behavior at frequencies compatible with the scale length of the topographic features (e.g., basins, hill shapes, orographic profiles, etc.). It follows that realistic descriptions of topography should definitely be included in seismological modeling. Inclusion of 3D heterogeneities (see the m3D case in Fig. 8), although approximate because our knowledge of the subsurface is often scanty, still contributes consistently to a reduction in amplitude misfits. However, for some stations, as already discussed in the previous section, model m3D tends to overestimate waveforms. This is mainly evident in the time windows that span vertical component coda, where model m1DT generally already gives a decent amplitude fit.

The trend of the amplitude misfit is also represented in Figure 10a,c. The cumulative distribution of windows as a function of the absolute value of $\Delta \ln A$ (Fig. 10a) shows a sensible increment of the window number for lower values of $\Delta \ln A$ when models m1DT or m3D are used, complemented by a reduction of the maximum abs($\Delta \ln A$) in these cases. The amplitude measurement distribution (Fig. 10c) tends to be centered on zero for models m1DT and m3D, reducing the number of windows with large amplitude differences. Figure 10c also highlights the tendency of model m3D to overestimate the observed traces in many windows.

Regarding the behavior of travel-time misfit for different structural models, Figure 9 does not show a clear common trend and the variations of ΔT strongly depend on the choice of window. Topography and 3D heterogeneities have a complex effect on phase arrivals of full synthetic waveforms, producing in many cases lower values of the misfit (e.g., in Fig. 9, model m1DT for the N component of station AQK, the east [E] and north [N] components of station AVZ, the vertical [*Z*] component of station NRCA, the E component of station CERA, or model m3D for the N component of station CAMP, the *Z* component of station RMP, the N component of station MA9, the N and *Z* components of station VAGA). In other cases, however, models m1DT or m3D seem to deteriorate the travel-time fit with respect to model m1DF, both increasing and decreasing ΔT (e.g., in Fig. 9, model m1DT for some windows of SPO N and of SPC E, or model m3D for some windows of NRCA N and a window of AVZ N).

From the cumulative distribution in Figure 10b one cannot deduce characteristic behavior of the travel-time misfit for different models. Moreover, as shown in Figure 10d, travel-time measurement distributions for all models are spread over a relatively large range of values and are not centered on zero. Therefore, the results of the travel-time misfit analysis shown in Figures 9 and 10b–d do not allow us to draw general conclusions about phase behavior. In this case, direct visual comparisons of observed and synthetic waveforms are better suited for identifying the capabilities of models with topography and 3D heterogeneities in reproducing features in observed seismograms. What is highlighted by Figures 3–5 is that the complexities of recorded waveforms require a 3D structural description with topography.

It is worth remarking that the introduction of a 3D model can lead to the generation of amplitudes larger than those observed in the data, especially when a simpler 1D model with topography already provides a reasonable fit. Scognamiglio *et al.* (2010) reduced M_w of the 2009 L'Aquila event from 6.3 to 6.1 because an overestimation of slip produced strongly amplified waveforms in simulated time series. This reduction is quite plausible, noting that the results of our simulations based on the 3D model are intrinsically affected by a possible incompatibility between source and structural models. Whereas we use a 3D wavespeed model constructed based on tomography, the source model of Cirella *et al.* (2009) is obtained by an inversion based on a 1D flat wavespeed profile. This important source of discrepancy between data and synthetics could be resolved in the future by exploiting finite-source models in combination with 3D structural models (e.g., Trasatti *et al.*, 2011; Volpe *et al.*, 2012). Concerning the debate about magnitude, we emphasize that its estimate is not independent from the chosen structural model.

The fact that many features in observed seismograms are either missing or poorly matched by the 3D model also highlights that a more accurate description of the structure is required. In constructing our 3D model for central Italy we

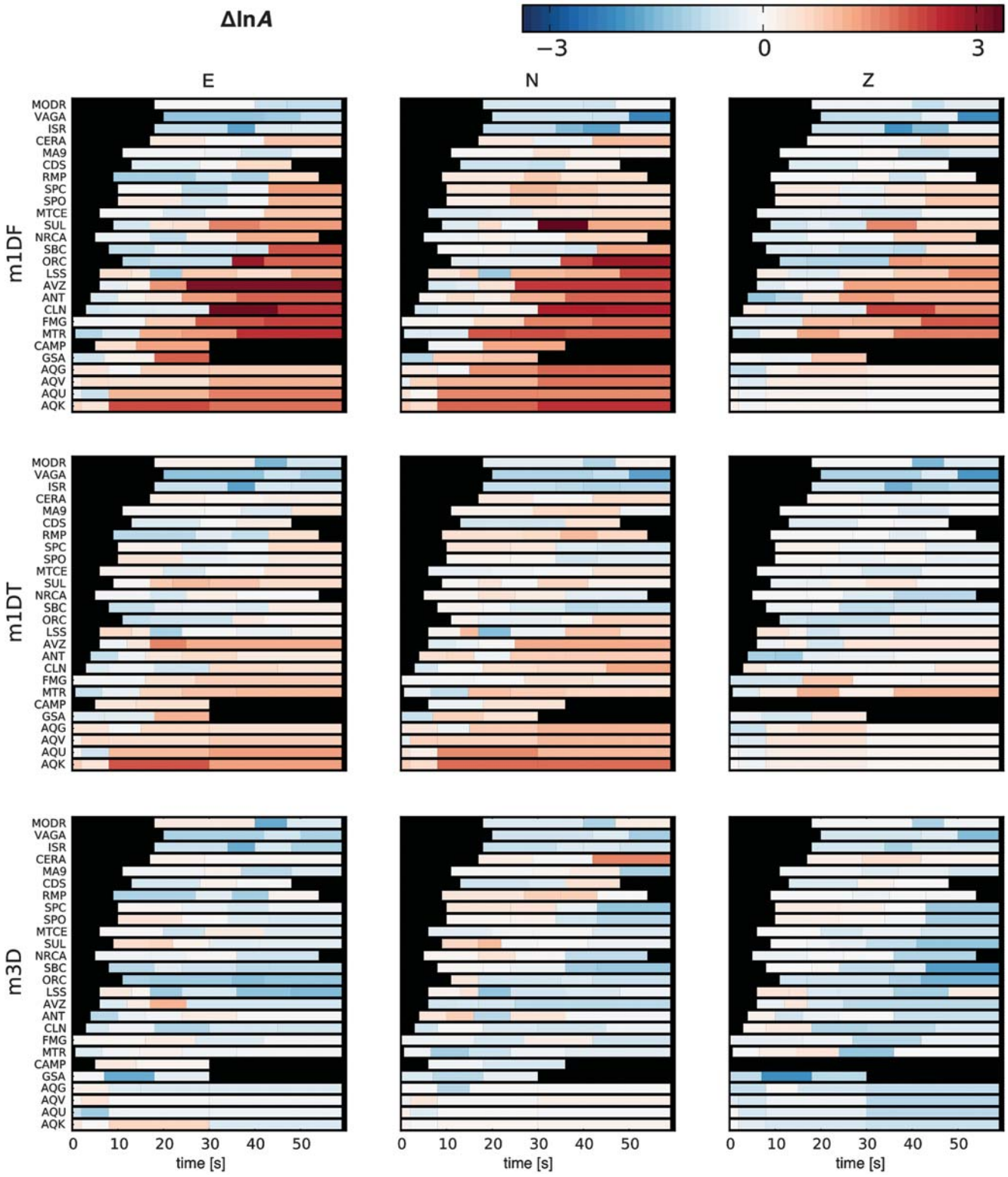

Figure 8. Cross-correlation amplitude differences $\Delta \ln A$ (equation 1 in the text) between observed and SEM synthetic waveforms for all stations. Labels on the left refer to the wavespeed model used to simulate the synthetics with *SPECFEM3D_Cartesian*: m1DF is for the 1D wavespeed model without topography, m1DT for the 1D model with topography, and m3D for the 3D model. Bars for each model (m1DF, m1DT, m3D), component, and station indicate the manually selected time windows within which we compare data and synthetics; the colors define the calculated values of the amplitude difference in a given window. Based on equation (1) in the text, positive values of $\Delta \ln A$ indicate that the synthetic seismogram underestimates the observed one, so the color tends to red. On the other hand, negative values of $\Delta \ln A$ (blue color) correspond to overestimating observed waveforms. When the color approaches white, the amplitude misfit approaches zero and the fit improves.

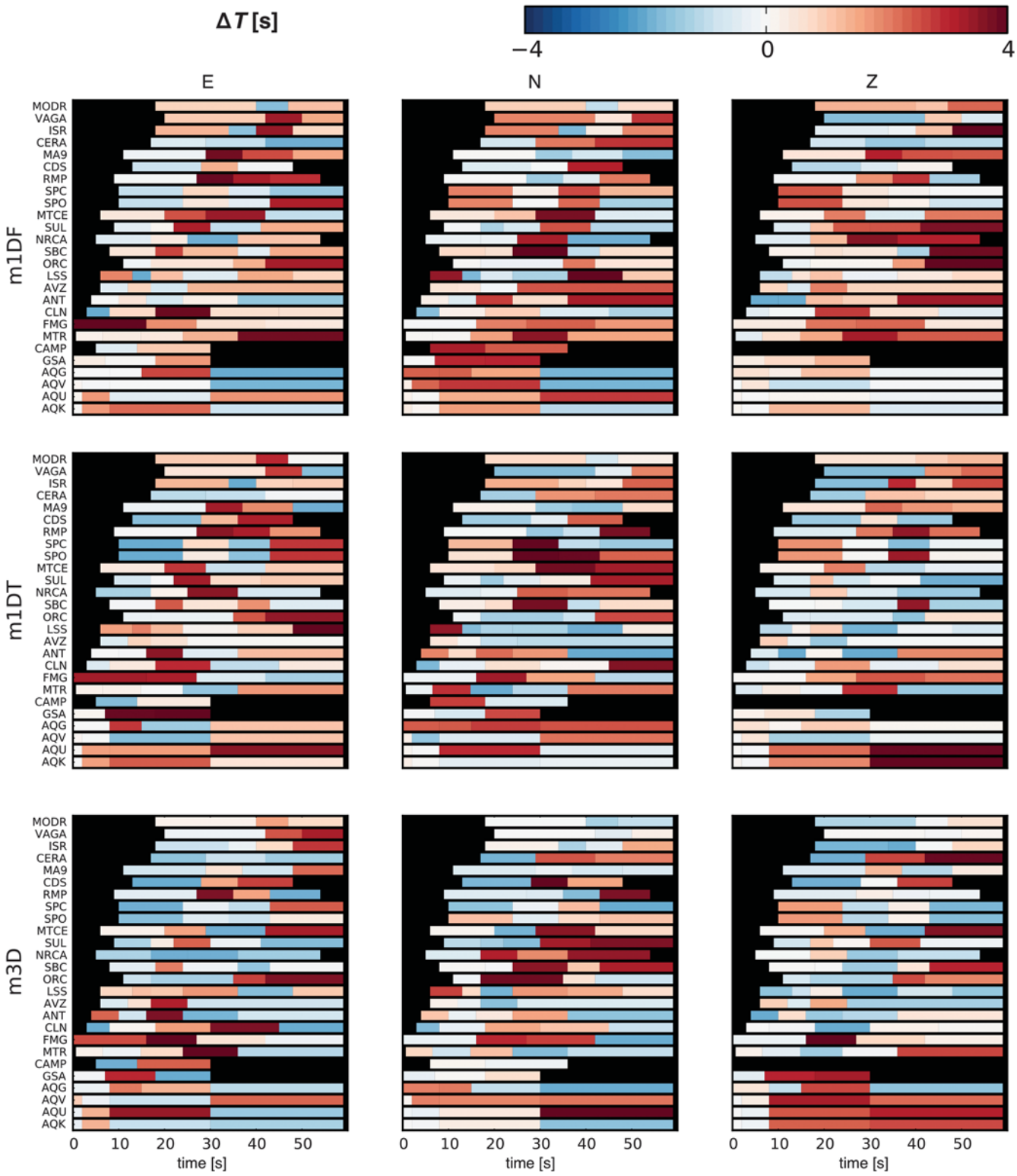

Figure 9. Same as Figure 8, but for cross-correlation travel-time difference (in s) between data and SEM synthetics (equation 2 in the text). Positive values (red) mean that the synthetics are early compared to the observations, so the wavespeed model is too fast; the reverse is true for negative values (blue).

seek to introduce all available information. However, the adopted wavespeed profiles are possibly affected by uncertainties implicit in the tomographic technique. In particular, basin effects are accounted for by superimposing the V_{S30} layer on top of the tomographic model. The frequency range of our study and the dimensions of the model justify the use of V_{S30}, while simplifying and accelerating the construction of the mesh required for the simulations. However, in order

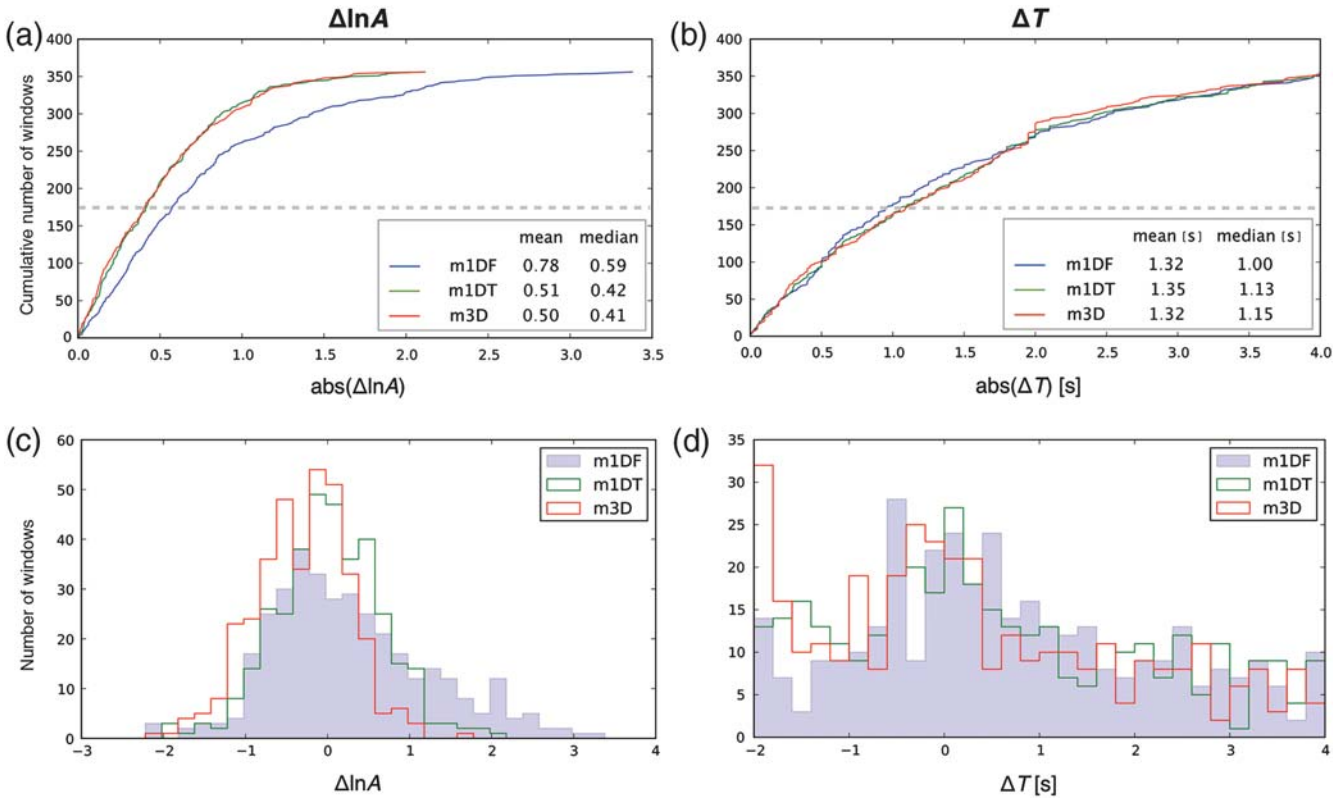

Figure 10. (a) Cumulative number of time windows as a function of the absolute value of the cross-correlation amplitude difference, abs($\Delta \ln A$), between data and SEM synthetics for the 1D flat model (m1DF), the 1D model with topography (m1DT), and the 3D model (m3D). All stations and components are taken into account. The mean and median values for each wavespeed model are shown in the legend, and the dashed gray line highlights the median for each model. (b) Same as (a), but for the cross-correlation travel-time difference (in s). (c) Distributions of the cross-correlation amplitude difference for the three wavespeed models (m1DF, m1DT, m3D), considering all 26 stations and three-component ground motions. (d) Same as (c), but for the cross-correlation travel-time difference (in s).

to increase the frequency content of the simulations, a refinement of the model within basins is necessary. This requires the definition of their shapes and wavespeed contrasts, and possibly honoring these features within the mesh (e.g., Lee *et al.*, 2008). Future analyses of the 2009 L'Aquila event may use a more detailed structural description, for example, an improved 3D model obtained from adjoint tomography (Magnoni, 2012).

With regards to attenuation, our simulations with models m1DT and m3D are based on a simplified description of the quality factor, due to the lack of an accurate, comprehensive model for Q in central Italy. However, our results suggest that incorporating attenuation using the Olsen *et al.* (2003) model improves the fit to observed data with respect to a completely elastic model.

A possible limitation of our simulations is that we did not include nonlinearity. This effect may become relevant especially at short distances from the seismic source and could help to reduce the discrepancies between data and synthetics. However, we believe that the frequencies considered in this work are too low to see significant nonlinear effects, although specific analyses would be required to prove that these effects are negligible in our frequency range. Another possible limitation is that only a kinematic source model is considered. Thus, a dynamic rupture model, which can be handled by *SPECFEM3D_Cartesian* as well (e.g., Madariaga *et al.*, 2006; Huang *et al.*, 2013), could be helpful in future work to better capture the source complexity that affects the waveforms.

Ground motions induced by the 2009 M_w 6.3 L'Aquila earthquake were recently studied by Smerzini and Villani (2012). They produced SEM synthetics numerically accurate up to 2.5 Hz and highlight the role of stochastically varying kinematic source parameters in exciting higher-frequency ground motions, with the ultimate objective of reconstructing broadband near-fault wavefields for engineering purposes. Their implementation of the SEM in the code *GeoELSE* (following Faccioli *et al.*, 1997) is somewhat different from the *SPECFEM3D_Cartesian* implementation, allowing, for example, for nonlinear viscoplastic models (di Prisco *et al.*, 2007) or source parameters described as stochastic spatial fields. In addition, instead of a tomographic description of the structure, Smerzini and Villani (2012) constructed a 3D wavespeed model by considering an approximate 3D shape of the Aterno Valley, a horizontally layered crustal model and a linear viscoelastic material. The simulated region is

considerably smaller than our model volume, and the main focus of their work is to test different finite-source models with the same geological structure. It is worth noting that for frequencies up to ~0.5 Hz our 3D synthetics, as well as those of Smerzini and Villani (2012) for the same strong-motion stations (see their table 1), decently fit observed waveforms, and maps of PGV are in good agreement with observed values (see the next section). In particular, limiting the maximum frequency to ~0.5 Hz, ground-motion amplitudes for stations in the upper Aterno Valley, such as AQV and AQG, which are underestimated in the study by Smerzini and Villani (2012), are well reproduced using our 3D structure model (see model m3D in Fig. 8).

Peak Ground Velocities

PGV maps can be very useful to construct hazard scenarios, highlighting ground-motion features in surrounding areas. Many studies document increased peak ground acceleration (PGA) and PGV due to the presence of sedimentary basins and also due to the source radiation pattern (e.g., Komatitsch *et al.*, 2004; Lee *et al.*, 2008; Lee, Chan, *et al.*, 2009; Lee, Komatitsch, *et al.*, 2009; Stupazzini *et al.*, 2009, and references therein). Some of them (Lee *et al.*, 2008; Lee, Chan, *et al.*, 2009; Lee, Komatitsch, *et al.*, 2009) infer a variation of the expected PGA and PGV related to topography. Thus, they suggest that a high-resolution realistic topography description should be considered in seismic-hazard analysis, especially for densely populated mountainous areas, as advocated by numerous other studies (e.g., Komatitsch and Vilotte 1998; Massa *et al.*, 2010, and references therein). Concerning central Italy, the zone struck by the 2009 L'Aquila event is characterized by high levels of seismic hazard (MPS, Gruppo di Lavoro 2004). The maximum observed value of PGV in the epicentral area, inferred from RAN and INSN station recordings, is ~65 cm/s (see Data and Resources). Moreover, prominent source directivity toward the southeast was deduced for the 2009 L'Aquila earthquake (e.g., Pino and Di Luccio, 2009; Akinci *et al.*, 2010, and references therein), causing a systematic decrease of PGA and PGV values at sites located to the northwest, that is, in the opposite direction of the rupture propagation (compared to sites located to the southeast). This is consistent with the asymmetric rupture velocity inferred by Cirella *et al.* (2009).

This section presents synthetic maps of PGV obtained by considering both 1D velocity models (m1DF and m1DT) and the 3D model, together with the corresponding finite source. Figure 11a–c shows the three maps, highlighting the effects of introducing topography and 3D lateral heterogeneities. The observed values of PGV at RAN and INSN stations are indicated by the circles in the figures, based on the color scale.

Considering the m1DF model, the observed values of PGV are in general underestimated (Fig. 11a). In the epicentral area the maximum value is 45 cm/s, about 30% lower than observed. Introduction of topography (and attenuation) in the model results in a better agreement between observed and estimated PGV values (Fig. 11b). In particular, the topographic ridges are highlighted, for example, along the Gran Sasso massif in the northeast, featuring higher values of PGV with respect to model m1DF. An interesting case is station GSA, which is located in a small sedimentary plateau and its PGV value was overestimated by model m1DF. When topography is included, the PGV at this station is better reproduced. The maximum calculated PGV value at the epicenter is 48 cm/s. Finally, when using model m3D (Fig. 11c), we obtain PGV estimates in satisfactory agreement with observed values, and in the epicentral area the maximum PGV is 74 cm/s. In this case topographic effects are still evident, and, in addition, the highest values of PGV are mainly observed in sedimentary basins, where most of the energy is trapped. The estimate of PGV at station AVZ in the Fucino basin is improved with respect to the 1D cases. In all maps a source directivity effect on the PGV distribution is evident, with higher values toward the southeast, however model m3D is particularly able to reproduce this aspect.

Based on the obtained results, as expected, the pattern of PGV values is strongly influenced by the inclusion of topography and 3D heterogeneities. A better agreement with the observed estimates can be obtained by accounting for all structural complexities. This leads us to conclude that very accurate descriptions of topography and wavespeed heterogeneities (e.g., basins, ridges, etc.) are essential for modeling PGV and PGA.

The synthetic maps produced by *SPECFEM3D_Cartesian* can be used to construct synthetic ShakeMaps that complement the empirically derived ShakeMaps for the ground-motion intensity in central Italy (Michelini *et al.*, 2008). For the 2009 L'Aquila event, the empirically obtained ShakeMap (see Faenza *et al.*, 2011; and Data and Resources) is shown in Figure 11d.

3D Adjoint Sensitivity Kernels

It has been shown that synthetic seismograms simulated using models m1DT and m3D can accurately reproduce particular features (e.g., later arrivals in the coda due to 3D heterogeneity) in observed waveforms. The adjoint approach (e.g., Tarantola, 1984; Tromp *et al.*, 2005, 2008; Fichtner, 2010) may be used to illuminate the volumetric sensitivity region for specific seismic pulses (e.g., Tape *et al.*, 2010) via finite-frequency sensitivity kernels. These kernels are obtained from the interaction of a regular wavefield, generated by the earthquake, and an adjoint wavefield, generated by considering time-reversed signals at the receivers as sources (e.g., Liu and Tromp, 2006; Tape *et al.*, 2007). Running the forward and adjoint simulations together yields sensitivity associated with the chosen waveform, and its sensitivity is reflected by the kernels (e.g., Tromp *et al.*, 2008). Following Tromp *et al.* (2005), the variation of a generic misfit function F may be written in terms of these volumetric kernels. In particular, for an isotropic model parametrized in terms of compressional wavespeed α, shear wavespeed

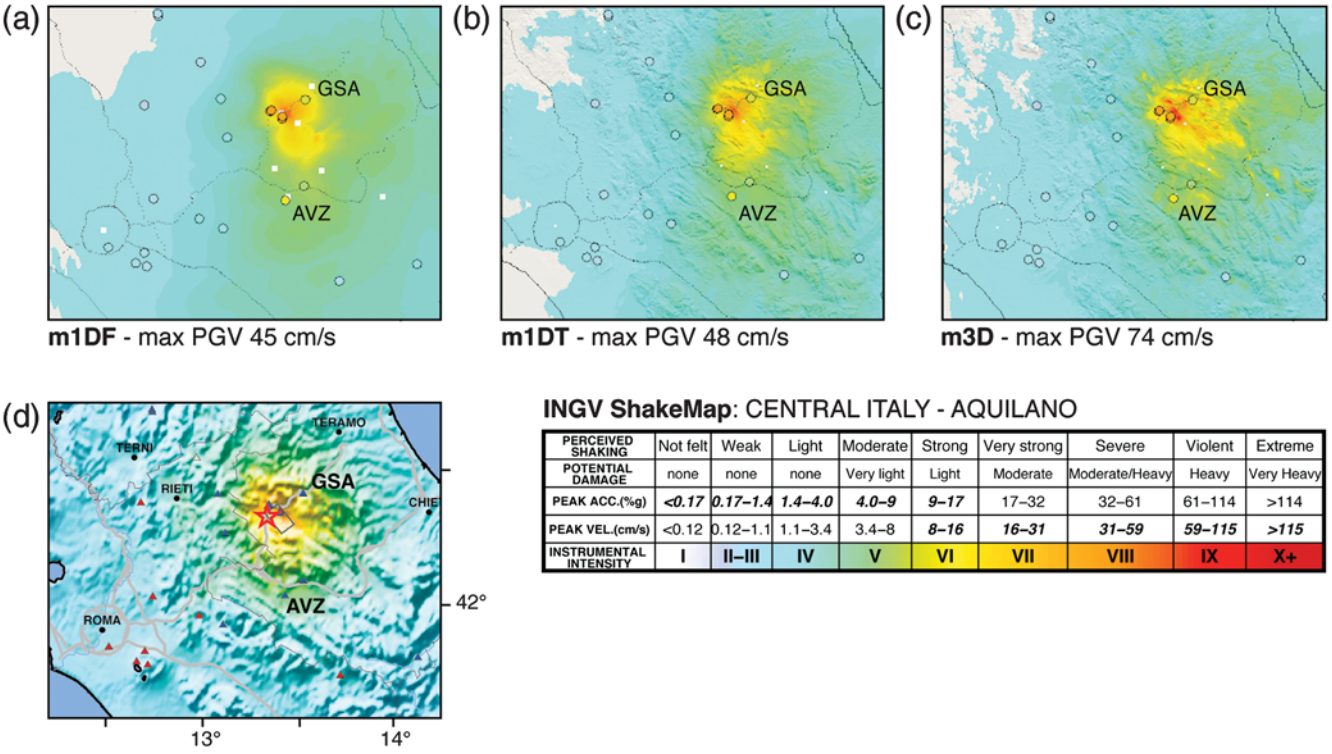

Figure 11. (a)–(c) Synthetic PGV maps obtained using *SPECFEM3D_Cartesian* with the finite-fault model for the 2009 M_w 6.3 L'Aquila event and three different wavespeed models: (a) 1D wavespeed model without topography (m1DF), (b) 1D model with topography (m1DT), and (c) 3D model (m3D). Circles show PGV values observed at RAN and INSN stations. The maximum PGV indicated in each panel is the highest value in the epicentral area. Colors refer to PGV values based on the scale on the bottom right. (d) ShakeMap of ground motion in central Italy, generated by the 2009 L'Aquila event (see Faenza *et al.*, 2011). Considering the scale on the right, colors correspond to PGV values and also to other parameter ranges (e.g., PGA and instrumental intensity), based on Wald *et al.* (1999).

$$\delta F = \int_V (K'_\rho \delta \ln \rho + K_\alpha \delta \ln \alpha + K_\beta \delta \ln \beta) \mathrm{d}^3\mathbf{x}, \qquad (3)$$

β, and density ρ, one may write in which the integral is over the model volume V.

In equation (3), the isotropic misfit kernels K_α and K_β are the Fréchet derivatives with respect to relative perturbations in compressional and shear wavespeeds, respectively, and are expressed as

$$K_\alpha = 2\left(\frac{\kappa + \frac{4}{3}\mu}{\kappa}\right) K_\kappa, \qquad K_\beta = 2\left(K_\mu - \frac{4}{3}\frac{\mu}{\kappa} K_\kappa\right), \qquad (4)$$

in which the isotropic misfit kernels K_μ and K_κ for the shear and bulk moduli are

$$K_\mu = -2\mu \int_0^T \mathbf{D}^\dagger(T-t) : \mathbf{D}(t) \mathrm{d}t,$$
$$K_\kappa = -\kappa \int_0^T [\nabla \cdot \mathbf{s}^\dagger(T-t)][\nabla \cdot \mathbf{s}(t)] \mathrm{d}t, \qquad (5)$$

with $\mathbf{D} = \frac{1}{2}[\nabla \mathbf{s} + (\nabla \mathbf{s})^T] - \frac{1}{3}(\nabla \cdot \mathbf{s})\mathrm{I}$ and $\mathbf{D}^\dagger = \frac{1}{2}[\nabla \mathbf{s}^\dagger + (\nabla \mathbf{s}^\dagger)^T] - \frac{1}{3}(\nabla \cdot \mathbf{s}^\dagger)\mathrm{I}$ the traceless strain deviator and its adjoint, respectively. Then

$$K'_\rho = K_\kappa + K_\mu + K_\rho \quad \text{with}$$
$$K_\rho = -\rho \int_0^T \mathbf{s}^\dagger(T-t) \cdot \partial_t^2 \mathbf{s}(t) \mathrm{d}t. \qquad (6)$$

As an example, and to highlight the effects of topography and 3D heterogeneities on waveforms, we construct the travel-time adjoint source for a kernel calculation using the signal within the 30–40 s time window of the vertical component velocity at station SUL (Fig. 12, bottom left). The forward wavefield is obtained using *SPECFEM3D_Cartesian* with the finite-fault model for the 2009 L'Aquila earthquake and the 3D structural model that also includes topography; the code is subsequently used to perform the adjoint simulation and to construct the kernels. The resulting impedance sensitivity kernel K'_ρ is shown in Figure 12. In the selected frequency band (0.02 Hz–0.5 Hz), the kernel shows that the sensitivity is mainly concentrated along the Gran Sasso and Maiella Massifs, carefully following the path of the ridges. Residual sensitivities occur in the source and receiver regions, a common feature of sensitivity kernels, whereas the slow wavespeed features attributed to the numerous sedimentary basins in central Italy are largely avoided. This reveals, as expected, a strong influence of both topography and 3D heterogeneities on controlling seismic-wave propagation. In particular, it suggests that the specific pulse

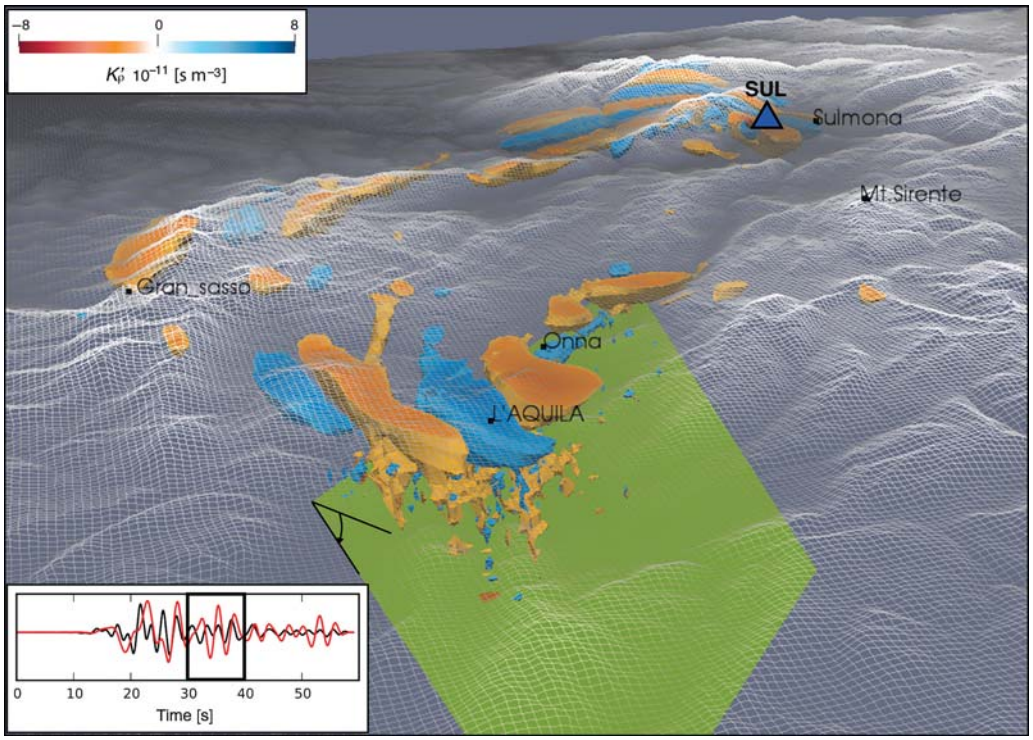

Figure 12. Impedance 3D sensitivity kernel K'_ρ, viewed from the northwest, for the signal within the black outlined time window in the bottom left picture. Seismograms represent Z-component velocity (in cm/s) at station SUL (blue triangle): data are in black, and synthetics simulated using *SPECFEM3D_Cartesian* and the 3D wavespeed model are in red. The adjoint source for the kernel calculation was constructed using the time-reversed synthetic velocity within the selected time window. The frequency range is 0.02–0.5 Hz. The fault plane for the 2009 M_w 6.3 L'Aquila earthquake is shown in green.

selected on the seismogram at SUL is mostly sensitive to topographic effects. These areas of high sensitivity can be attributed to topographic scattering and multiple reflections that affect the signal within the chosen window.

Conclusions and Future Work

In this study, we have simulated the wavefield generated by the 2009 M_w 6.3 L'Aquila earthquake, using a spectral-element method in combination with a kinematic finite-fault solution and various wavespeed models, both 1D and 3D. Using the SEM software package *SPECFEM3D_Cartesian*, we consider complexities that influence seismic ground motion (e.g., 3D structural heterogeneities, topography, attenuation, fault finiteness). We have confirmed that the SEM is a very powerful tool for accurately simulating observed ground motions in the near-source region of moderate to large earthquakes characterized by complex rupture processes in complicated geological settings. The simulations highlight a strong sensitivity to 3D geological features, which are generally ignored in the inversion for seismological source parameters. In particular, our results demonstrate that many of the pulses in the recorded traces can be reproduced up to ~0.5 Hz by including topography and 3D structural heterogeneities.

Topography can produce significant waveform scattering, amplification, and multiple reflections. These effects are visible in all seismograms at all stations, especially in their coda. Moreover, although dominated by the characteristics of the source, first arrivals are affected in amplitude by the presence of steep topography. Synthetic seismograms start to match observed traces reasonably well when topography is superimposed on a 1D structural model (model m1DT). We conclude that realistic simulations of wave propagation in central Italy require consideration of topographic scattering. We used an adjoint analysis to illustrate that the origin of distinct features in observed seismograms is not necessarily confined to isolated parts of the structural model, rather it is often the result of a combination of multiple structural characteristics for a given source–receiver geometry.

Effects of alluvial basins are captured only partially by our simulations. In particular, stations in larger basins exhibit more accurate waveform fits than those located in or close to smaller ones. This suggests that we likely overestimated the vertical dimension of the smaller basins and thus their impact on the seismograms. Although our synthetics capture important characteristics of observed seismograms, they do not account for many other arrivals and often overestimate amplitudes. This indicates that the adopted structural model needs refinement, because many features of the real structure are likely poorly constrained or neglected. In addition, the larger amplitudes observed in the synthetics when compared to the data can be ascribed to overestimates of the on-fault

slip which, we recall, was obtained from an inversion that adopted a 1D wavespeed profile as the structural model. It follows that there is an intrinsic incompatibility between the source and structural models.

Our analysis confirms that alluvial basins and their associated complex geology can have a strong impact in terms of seismic hazard. Specifically, our 3D model, together with the finite-fault representation, significantly improves fits between observed and synthetic estimates of PGV for the 2009 L'Aquila event. Inclusion of both low wavespeed basins and topography increases PGV and generally improves the match to observed values. This demonstrates that both topography and 3D structure represent fundamental information when earthquake scenarios are used for seismic-hazard assessment.

In the future it is expected that full waveform tomography of the central Apennines will result in an improved 3D structural model, thereby facilitating the determination of more accurate and detailed finite-fault slip models, resulting in more accurate 3D Green's functions. This will require expansion of computational resources and power, thereby overcoming current frequency limitations with fundamental consequences for seismic-hazard studies.

Data and Resources

Numerical simulations were performed using the spectral-element code *SPECFEM3D_Cartesian* (http://www.geodynamics.org, last accessed September 2013). Travel time and amplitude misfit measurements were made using the code *measure_adj* (http://www.geodynamics.org, last accessed September 2013). Meshes for the numerical simulations were constructed using the *CUBIT* mesh generation package (http://cubit.sandia.gov, last accessed September 2013). Seismograms recorded at velocimetric stations of INSN are available upon request via http://eida.rm.ingv.it (European Integrated Data Archive [EIDA], managed by INGV; last accessed September 2013); waveforms recorded by MedNet are available upon request via http://mednet.rm.ingv.it (last accessed September 2013). Strong-motion data recorded by RAN were obtained from the ITalian ACcelerometric Archive (ITACA), available at http://itaca.mi.ingv.it/ItacaNet/ (last accessed September 2013). The Time Domain Moment Tensor (TDMT) solution for the 2009 L'Aquila earthquake was obtained from the INGV online archive, available via http://cnt.rm.ingv.it/tdmt.html (last accessed September 2013). The empirically derived ShakeMap for the mainshock and PGV values at RAN and INSN stations are available via http://shakemap.rm.ingv.it (last accessed September 2013). All other data used in this article come from published studies cited in the references.

Acknowledgments

The authors thank the managers of INGV High-Performance Computing (HPC) resources in Rome for allowing use of the cluster ELIOS and supplying useful technical support. We are grateful to Antonella Cirella, Claudio Chiarabba, Raffaele Di Stefano, Laura Scognamiglio, Elisa Tinti, Francesco Pio Lucente, Licia Faenza, Antonio Rovelli, and Marta Pischiutta for their contribution and fruitful discussions. We also thank the editor and the two anonymous reviewers for their comments and useful suggestions. This study has been partly supported by the EC n. 283543 VERCE project.

References

Acosta Minolia, C. A., and D. A. Kopriva (2011). Discontinuous Galerkin spectral element approximations on moving meshes, *J. Comput. Phys.* **230,** no. 5, 1876–1902

Akçelik, V., J. Bielak, G. Biros, I. Epanomeritakis, A. Fernandez, O. Ghattas, E. J. Kim, J. Lopez, D. O'Hallaron, T. Tu, and J. Urbanic (2003). High-resolution forward and inverse earthquake modeling on terascale computers, in *SC'03: Proc. of the 2003 ACM/IEEE conference on Supercomputing*, Phoenix, Arizona, 15–21 November 2003, 52–72.

Akinci, A., L. Malagnini, and F. Sabetta (2010). Characteristics of the strong ground motions from the 6 April 2009 L'Aquila earthquake, Italy, *Soil Dynam. Earth. Eng.* **30,** 320–335.

Ameri, G., M. P. Massa, D. Bindi, E. DAlema, A. Gorini, L. Luzi, S. Marzorati, F. Pacor, R. Paolucci, R. Pugli, and C. Smerzini (2009). The April 6 2009, M_w 6.3 L'Aquila (central Italy) earthquake: Strong-motion observations, *Seismol. Res. Lett.* **80,** 951–966.

Anzidei, M., E. Boschi, V. Cannelli, R. Devoti, A. Esposito, A. Galvani, D. Melini, G. Pietrantonio, F. Riguzzi, V. Sepe, and E. Serpelloni (2009). Coseismic deformation of the destructive April 6, 2009 L'Aquila earthquake (central Italy) from GPS data, *Geophys. Res. Lett.* **36,** L17307, doi: 10.1029/2009GL039145.

Arnold, D. N. (1982). An interior penalty finite element method with discontinuous elements, *SIAM J. Numer. Anal.* **19,** no. 4, 742–760.

Atzori, S., I. Hunstad, M. Chini, S. Salvi, C. Tolomei, C. Bignami, S. Stramondo, E. Trasatti, A. Antonioli, and E. Boschi (2009). Finite fault inversion of DInSAR coseismic displacement of the 2009 L'Aquila earthquake (central Italy), *Geophys. Res. Lett.* **36,** L15305, doi: 10.1029/2009GL039293.

Bagh, S., L. Chiaraluce, P. De Gori, M. Moretti, A. Govoni, C. Chiarabba, P. Di Bartolomeo, and M. Romanelli (2007). Background seismicity in the central Apennines of Italy: The Abruzzo region case study, *Tectonophysics* **444**, no. 1–4, 80–92.

Bao, H., J. Bielak, O. Ghattas, L. F. Kallivokas, D. R. O'Hallaron, J. R. Shewchuk, and J. Xu (1998). Large-scale simulation of elastic wave propagation in heterogeneous media on parallel computers, *Comput. Meth. Appl. Mech. Eng.* **152,** 85–102.

Bindi, D., R. Castro, G. Franceschina, L. Luzi, and F. Pacor (2004). The 1997–1998 Umbria-Marche sequence (central Italy): Source, path, and site effects estimated from strong motion data recorded in the epicentral area, *J. Geophys. Res.* **109,** no. B4, B04312, doi: 10.1029/2003JB002857.

Bindi, D., F. Pacor, L. Luzi, M. Massa, and G. Ameri (2009). The M_w 6.3, 2009 L'Aquila earthquake: Source, path and site effects from spectral analysis of strong motion data, *Geophys. J. Int.* **179,** 1573–1579.

Bosi, C., and T. Bertini (1970). Geologia della media valle dellAterno, *Mem. Soc. Geol. Ital.* **IX,** 719–777.

Bouchon, M., and J. S. Barker (1996). Seismic response of a hill: The example of Tarzana, California, *Bull. Seismol. Soc. Am.* **86,** no. 1A, 66–72.

Bouchon, M., C. A. Schultz, and M. N. Töksoz (1996). Effect of three-dimensional topography on seismic motion, *J. Geophys. Res.* **101,** 5835–5846.

Carcione, J. M. (1994). The wave equation in generalized coordinates, *Geophysics* **59,** 1911–1919.

Casarotti, E., M. Stupazzini, S. Lee, D. Komatitsch, A. Piersanti, and J. Tromp (2008). CUBIT and seismic wave propagation based upon the spectral-element method: An advanced unstructured mesher for complex 3D geological media, in *Proc. of the 16th International Meshing Roundtable*, Vol. 5B.4, 579–597.

Castro, R., F. Pacor, D. Bindi, G. Franceschina, and L. Luzi (2004). Site response of strong motion stations in the Umbria, central Italy, region, *Bull. Seismol. Soc. Am.* **94,** 576–590.

Cavinato, G. P., and P. G. De Celles (1999). Extensional basins in the tectonically bimodal central Apennines fold-thrust belt, Italy: Response to corner flow above subducting slab retrograde motion, *Geology* **27,** 955–958.

Çelebi, M. (1987). Topographical and geological amplifications determined from strong-motion and aftershock records of the 3 March 1985 Chile earthquake, *Bull. Seismol. Soc. Am.* **77,** 1147–1167.

Çelebi, M., P. Bazzurro, L. Chiaraluce, P. Clemente, L. Decanini, A. DeSortis, W. Ellsworth, A. Gorini, E. Kalkan, S. Marcucci, G. Milana, F. Mollaioli, M. Olivieri, R. Paolucci, D. Rinaldis, A. Rovelli, F. Sabetta, and C. Stephens (2010). Recorded motions of the 6 April 2009 M_w 6.3 L'Aquila, Italy, earthquake and implications for building structural damage: Overview, *Earthq. Spectra* **26,** 651–684.

Chaljub, E. (2009). Spectral-element modeling of 3D wave propagation in the Alpine valley of Grenoble, France, in *ESG 2006, Third Third International Symposium on the Effects of Surface Geology on Seismic Motion*, P.-Y. Bard, E. Chaljub, C. Cornou, F. Cotton, and P. Guéguen, 30 August–1 September 2006, Vol. 2, LCPC Editions, 1467–1473.

Chaljub, E., and B. Valette (2004). Spectral element modelling of three-dimensional wave propagation in a self-gravitating Earth with an arbitrarily stratified outer core, *Geophys. J. Int.* **158,** 131–141.

Chaljub, E., D. Komatitsch, J. P. Vilotte, Y. Capdeville, B. Valette, and G. Festa (2007). Spectral element analysis in seismology, in *Advances in Wave Propagation in Heterogeneous Media*, R.-S. Wu and V. Maupin (Editors), Advances in Geophysics, Vol. 48, Elsevier, Academic Press, London, United Kingdom 365–419.

Chaljub, E., P. Moczo, S. Tsuno, P.-Y. Bard, J. Kristek, M. Käser, M. Stupazzini, and M. Kristekova (2010). Quantitative comparison of four numerical predictions of 3D ground motion in the Grenoble valley, France, *Bull. Seismol. Soc. Am.* **100,** no. 4, 1427–1455.

Cheloni, D., M. D'Agostino, E. D'Anastasio, A. Avallone, S. Mantenuto, R. Giuliani, M. Mattone, S. Calcaterra, P. Gambino, and D. Dominici (2010). Coseismic and initial post-seismic slip of the 2009 M_w 6.3 L'Aquila earthquake, Italy, from GPS measurements, *Geophys. J. Int.* **181,** no. 3, 1539–1546.

Chiarabba, C., S. Bagh, I. Bianchi, P. De Gori, and M. Barchi (2010). Deep structural heterogeneities and the tectonic evolution of the Abruzzi region (Central Apennines, italy) revealed by microseismicity, seismic tomography, and teleseismic receiver functions, *Earth Planet. Sci. Lett.* **295,** 462–476, doi: 10.1016/j.epsl.2010.04.028.

Chiaraluce, L. (2012). Unravelling the complexity of Apenninic extensional fault systems: A review of the 2009 L'Aquila earthquake (Central Apennines, Italy), *J. Struct. Geol.* **42,** 2–18.

Chiaraluce, L., A. Amato, M. Cocco, C. Chiarabba, G. Selvaggi, M. D. Bona, D. Piccinini, A. Deschamps, L. Margheriti, F. Courboulex, and M. Ripepe (2004). Complex normal faulting in the Apennines thrust-and-fold belt: The 1997 seismic sequence in central Italy, *Bull. Seismol. Soc. Am.* 94**,** 99–116.

Cirella, A., A. Piatanesi, M. Cocco, E. Tinti, L. Scognamiglio, A. Michelini, A. Lomax, and E. Boschi (2009). Rupture history of the 2009 L'Aquila (Italy) earthquake from non-linear joint inversion of strong motion and GPS data, *Geophys. Res. Lett.,* **36,** L19304, doi: 10.1029/2009GL039795.

Cirella, A., A. Piatanesi, E. Tinti, M. Chini, and M. Cocco (2012). Complexity of the rupture process during the 2009 L'Aquila, Italy, earthquake, *Geophys. J. Int.* **190,** 607–621.

Clouser, R. H., and C. A. Langston (1995). Modeling observed $P-R_g$ conversions from isolated topographic features near the NORESS array, *Bull. Seismol. Soc. Am.* **85,** 859–873.

Cohen, G., P. Joly, and N. Tordjman (1993). Construction and analysis of higher-order finite elements with mass lumping for the wave equation, in *Proc. of the second international conference on mathematical and numerical aspects of wave propagation*, SIAM, Philadelphia, Pennsylvania, 7–10 June 1993, 152–160.

De Luca, G., S. Marcucci, G. Milana, and T. Sano (2005). Evidence of low-frequency amplification in the city of L'Aquila, central Italy, through a multidisciplinary approach including strong-and weak-motion data, ambient noise, and numerical modeling, *Bull. Seismol. Soc. Am.* **95,** no. 4, 1469–1481.

Di Luzio, E., G. Mele, M. M. Tiberti, G. P. Cavinato, and M. Parotto (2009). Moho deepening and shallow upper crustal delamination beneath the central Apennines, *Earth Planet. Sci. Lett.* **280,** 1–12.

di Prisco, C., M. Stupazzini, and C. Zambelli (2007). Nonlinear SEM numerical analyses of dry dense sand specimens under rapid and dynamic loading, *Int. J. Numer. Anal. Meth. Geomech.* **31,** 757–788.

Di Stefano, R., I. Bianchi, M. G. Ciaccio, G. Carrara, and E. Kissling (2011). Three-dimensional Moho topography in Italy: New constraints from receiver functions and controlled source seismology, *Geochem. Geophys. Geosys.* **12,** Q09006, doi: 10.1029/2011GC003649.

Di Stefano, R., C. Chiarabba, L. Chiaraluce, M. Cocco, P. De Gori, D. Piccinini, and L. Valoroso (2011). Fault zone properties affecting the rupture evolution of the 2009 (M_w 6.1) L'Aquila earthquake (central Italy): Insights from seismic tomography, *Geophys. Res. Lett.* **38,** doi: 10.1029/2011gl047365.

Doglioni, C. (1991). A proposal of kinematic modelling for *W*-dipping subductions—Possible applications to the Tyrrhenian-Apennines system, *Terra Nova* **3,** 423–434.

Doglioni, C. (1995). Geological remarks on the relationships between extension and convergent geodynamic settings, *Tectonophysics* **252,** 253–267.

Donati, S., F. Marra, and A. Rovelli (2001). Damage and ground shaking in the town of Nocera Umbra during Umbria-Marche, central Italy, earthquakes: The special effect of a fault zone, *Bull. Seismol. Soc. Am.* **91,** 511–519.

EMERGEO Working Group (2010). Evidence for surface rupture associated with the M_w 6.3 L'Aquila earthquake sequence of April 2009 (central Italy), *Terra Nova* **22,** 43–51.

Faccioli, E., F. Maggio, R. Paolucci, and A. Quarteroni (1997). 2D and 3D elastic wave propagation by a pseudo-spectral domain decomposition method, *J. Seismol.* **1,** 237–251.

Faenza, L., V. Lauciani, and A. Michelini (2011). Rapid determination of the shakemaps for the L'Aquila main shock: A critical analysis, *Boll. Geof. Teor. Appl.* **52,** no. 3, 1–19.

Falk, R. S., and G. R. Richter (1999). Explicit finite element methods for symmetric hyperbolic equations, *SIAM J. Numer. Anal.* **36,** no. 3, 935–952.

Fichtner, A. (2010). *Full Seismic Waveform Modelling and Inversion*, Springer-Verlag, Heidelberg, Germany.

Herrmann, B., and L. Malagnini (2009). Systematic determination of moment tensor of the April 6th, 2009 L'Aquila earthquake sequence, in Abstract U23A-0029 presented at *2009 AGU Fall Meeting*, Vol. 90, San Francisco, California.

Hu, F. Q., M. Y. Hussaini, and P. Rasetarinera (1999). An analysis of the discontinuous Galerkin method for wave propagation problems, *J. Comput. Phys.* **151,** no. 2, 921–946.

Huang, Y., L. Meng, and J.-P. Ampuero (2013). A dynamic model of the frequency-dependent rupture process of the 2011 Tohoku-Oki earthquake, *Earth Planets Space* **64,** 1061–1066.

Hunstad, I., G. Selvaggi, N. DAgostino, P. England, P. Clarke, and M. Pierozzi (2003). Geodetic strain in peninsular Italy between 1875 and 2001, *Geophys. Res. Lett.* **30,** 1181.

Jarvis, A., H. Reuter, A. Nelson, and E. Guevara (2008). Hole-filled seamless SRTM data V4. Tech. rep., International Centre for Tropical Agriculture (CIAT), available at http://srtm.csi.cgiar.org (last accessed November 2013).

Käser, M., and M. Dumbser (2006). An arbitrary high order discontinuous Galerkin method for elastic waves on unstructured meshes I: The two dimensional isotropic case with external source terms, *Geophys. J. Int.* **166,** no. 2, 855–877.

Kawase, H., and K. Aki (1990). Topography effect at the critical *SV*-wave incidence: Possible explanation of damage pattern by the Whittier

Narrows, California, earthquake of 1 October 1987, *Bull. Seismol. Soc. Am.* **80,** 1–22.

Komatitsch, D. (1997). *Méthodes spectrales et éléments spectraux pour l'équation de l'élastodynamique 2D et 3D en milieu hétérogène (Spectral and spectral-element methods for the 2D and 3D elastodynamics equations in heterogeneous media)*, *Ph.D. Thesis*, Institut de Physique du Globe, Paris, France, 187 pp.

Komatitsch, D. (2011). Fluid-solid coupling on a cluster of GPU graphics cards for seismic wave propagation, *C. Roy. Acad. Sci., Ser. IIb Mec.,* **339,** 125–135.

Komatitsch, D., and J. Tromp (2002a). Spectral-element simulations of global seismic wave propagation-I. Validation, *Geophys. J. Int.* **149,** no. 2, 390–412.

Komatitsch, D., and J. Tromp (2002b). Spectral-element simulations of global seismic wave propagation-II. 3-D models, oceans, rotation, and self-gravitation, *Geophys. J. Int.* **150,** no. 1, 303–318.

Komatitsch, D., and J. P. Vilotte (1998). The spectral-element method: An efficient tool to simulate the seismic response of 2D and 3D geological structures, *Bull. Seismol. Soc. Am.* **88,** no. 2, 368–392.

Komatitsch, D., Q. Liu, J. Tromp, P. Süss, C. Stidham, and J. H. Shaw (2004). Simulations of ground motion in the Los Angeles basin based upon the spectral-element method, *Bull. Seismol. Soc. Am.* **94,** no. 1, 187–206.

Komatitsch, D., S. Tsuboi, and J. Tromp (2005). The spectral-element method in seismology, in *Seismic Earth: Array Analysis of Broadband Seismograms*, A. Levander and G. Nolet (Editors), American Geophysical Monograph, Vol. 157, Washington, D.C., 205–228.

Kopriva, D. A. (2006). Metric identities and the discontinuous spectral element method on curvilinear meshes, *J. Sci. Comput.* **26,** no. 3, 301–327.

Kopriva, D. A., S. L. Woodruff, and M. Y. Hussaini (2002). Computation of electromagnetic scattering with a non-conforming discontinuous spectral element method, *Int. J. Numer. Meth. Eng.* **53,** no. 1, 105–122.

Lee, S. J., Y. C. Chan, D. Komatitsch, B. S. Huang, and J. Tromp (2009). Effects of realistic surface topography on seismic ground motion in the Yangminshan region of Taiwan based upon the spectral-element method and LiDAR DTM, *Bull. Seismol. Soc. Am.* **99,** no. 2A, 681–693.

Lee, S. J., H. W. Chen, Q. Liu, D. Komatitsch, B. S. Huang, and J. Tromp (2008). Three-dimensional simulations of seismic wave propagation in the Taipei basin with realistic topography based upon the spectral-element method, *Bull. Seismol. Soc. Am.* **98,** no. 1, 253–264.

Lee, S. J., D. Komatitsch, B. S. Huang, and J. Tromp (2009). Effects of topography on seismic wave propagation: An example from northern Taiwan, *Bull. Seismol. Soc. Am.* **99,** no. 1, 314–325.

Li, H., A. Michelini, L. Zhu, F. Bernardi, and M. Spada (2007). Crustal velocity structure in Italy from analysis of regional seismic waveforms, *Bull. Seismol. Soc. Am.* **97,** no. 6, 2024–2039.

Liu, Q., and J. Tromp (2006). Finite-frequency kernels based on adjoint methods, *Bull. Seismol. Soc. Am.* **96**, no. 6, 2383–2397.

Liu, Q., J. Polet, D. Komatitsch, and J. Tromp (2004). Spectral-element moment tensor inversions for earthquakes in Southern California, *Bull. Seismol. Soc. Am.* **94,** no. 5, 1748–1761.

Lucente, F. P., P. De Gori, L. Margheriti, D. Piccinini, M. Di Bona, C. Chiarabba, and N. Piana Agostinetti (2010). Temporal variations of seismic velocity and anisotropy before the 2009 M_w 6.3 L'Aquila earthquake, Italy, *Geology* **38,** 1015–1018.

Madariaga, R. (1976). Dynamics of an expanding circular fault, *Bull. Seismol. Soc. Am.* **66,** no. 3, 639–666.

Madariaga, R., J.-P. Ampuero, and M. Adda-Bedia (2006). Seismic radiation from simple models of earthquakes, in *Radiated Energy and the Physics of Earthquakes*, A. McGarr, R. Abercrombie, H. Kanamori, and G. di Toro, (Editors) American Geophysical Monograph, Vol. 170, 223–236.

Magnoni, F. (2012). *Spectral-Element and Adjoint 3D Full-Wave Tomography for the Lithosphere of Central Italy, Ph.D. Thesis*, Università di Bologna Alma Mater Studiorum, Bologna, Italy.

Malinverno, A., and W. B. F. Ryan (1986). Extension in the Tyrrhenian Sea and shortening in the Apennines as result of arc migration driven by sinking of the lithosphere, *Tectonics* **5,** 227–245.

Mariucci, M. T., A. Amato, and P. Montone (1999). Recent tectonic evolution and present stress in the northern Apennines (Italy), *Tectonics* **18,** 108–118.

Marra, F., R. Azzara, F. Bellucci, A. Caserta, G. Cultrera, B. Mele, B. Palombo, A. Rovelli, and E. Boschi (2000). Large amplification of ground motion at rock sites within a fault zone in Nocera Umbra (central Italy), *J. Seismol.* **4,** 543–554.

Marzorati, S., C. Ladina, E. Falcucci, S. Gori, G. Ameri, D. Piccarreda, and F. Galadini (2009). Castelvecchio subequo (AQ): Evidenze di amplificazione sismica su roccia, in *Convegno Gruppo Nazionale Geofisica della Terra Solida-GNGTS*, Trieste, Italy.

Massa, M., S. Lovati, E. D'Alema, G. Ferretti, and M. Bakavoli (2010). An experimental approach for estimating seismic amplification effects at the top of a ridge, and the implication for ground-motion predictions: The case of Narni, central Italy, *Bull. Seismol. Soc. Am.* **100,** no. 6, 3020–3034.

Michelini, A., L. Faenza, V. Lauciani, and L. Malagnini (2008). ShakeMap implementation in Italy, *Seismol. Res. Lett.* **79,** 688–697.

Moczo, P., J. Robertsson, and L. Eisner (2007). The finite-difference time-domain method for modeling of seismic wave propagation, chapter 8 in *Advances in Wave Propagation in Heterogeneous Media*, R.-S. Wu and V. Maupin (Editors), Advances in Geophysics, Vol. 48, Elsevier, Academic Press, London, United Kingdom,, 421–516.

Monk, P., and G. R. Richter (2005). A discontinuous Galerkin method for linear symmetric hyperbolic systems in inhomogeneous media, *J. Sci. Comput.* **22–23,** no. 1–3, 443–477.

Monteiller, V., S. Chevrot, D. Komatitsch, and N. Fuji (2013). A hybrid method to compute short period synthetic seismograms of teleseismic body waves in a 3-D regional model, *Geophys. J. Int.* **192,** no. 1, 230–247, doi: 10.1093/gji/ggs006.

Montone, P., M. T. Mariucci, S. Pondrelli, and A. Amato (2004). An improved stress map for Italy and surrounding regions (central Mediterranean), *J. Geophys. Res.* **109,** B10410, doi: 10.1029/2003JB002703.

MPS, Gruppo di Lavoro (2004). Redazione della mappa di pericolosità sismica prevista dall'Ordinanza PCM del 20 marzo 2003, in *Rapporto Conclusivo per il Dipartimento dellaProtezione Civile, INGV*, Milano-Roma, Aprile 2004, pp. 65+5 appendices.

Olsen, K. B., and R. J. Archuleta (1996). 3-D simulation of earthquakes on the Los Angeles fault system, *Bull. Seismol. Soc. Am.* **86**, no. 3, 575–596.

Olsen, K. B., S. M. Day, and C. R. Bradley (2003). Estimation of Q for long-period (>2 sec) waves in the Los Angeles basin, *Bull. Seismol. Soc. Am.* **93,** no. 2, 627–638.

Olsen, K. B., S. Day, J. Minster, Y. Cui, A. Chourasia, M. Faerman, R. Moore, P. Maechling, and T. Jordan (2006). Strong shaking in Los Angeles expected from southern San Andreas earthquake, *Geophys. Res. Lett.* **33,** no. 7, 575–596.

Patacca, E., and P. Scandone (1989). The role of the passive sinking of a relic lithospheric slab, in *The Lithosphere in Italy* A. Boriani, M. Bonafede, P. G. Piccardo, and G. B. Vai (Editors), Academia Nazionale dei Lincei, Rome, 157–176.

Patacca, E., P. Scandone, E. Di Luzio, G. Cavinato, and M. Parotto (2008). Structural architecture of the central Apennines: Interpretation of the CROP 11 seismic profile from the Adriatic coast to the orographic divide, *Tectonics* **27,** TC3006, doi: 10.1029/2005TC001917.

Peter, D., D. Komatitsch, Y. Luo, R. Martin, N. Le Goff, E. Casarotti, P. Le Loher, F. Magnoni, Q. Liu, C. Blitz, T. Nissen-Meyer, P. Basini, and J. Tromp (2011). Forward and adjoint simulations of seismic wave propagation on fully unstructured hexahedral meshes, *Geophys. J. Int.* **186,** 721–739.

Piatanesi, A., A. Cirella, P. Spudich, and M. Cocco (2007). A global search inversion for earthquake kinematic rupture history: Application to the 2000 western Tottori, Japan earthquake, *J. Geophys. Res.* 112**,** B07314, doi: 10.1029/2006JB004821.

Pino, N. A., and F. Di Luccio (2009). Source complexity of the 6 April 2009 L'Aquila (central Italy) earthquake and its strongest aftershock revealed by elementary seismological analysis, *Geophys. Res. Lett.* **36,** L23305, doi: 10.1029/2009GL041331.

Pischiutta, M., G. Cultrera, A. Caserta, L. Luzi, and A. Rovelli (2010). Topographic effects on the hill of Nocera Umbra, central Italy, *Geophys. J. Int.* **182,** 977–987.

Priolo, E., J. M. Carcione, and G. Seriani (1994). Numerical simulation of interface waves by high-order spectral modeling techniques, *J. Acoust. Soc. Am.* **95,** no. 2, 681–693.

Rivière, B., and M. F. Wheeler (2003). Discontinuous finite element methods for acoustic and elastic wave problems, *Contemp. Math.* **329,** 271–282.

Rovelli, A., L. Scognamiglio, F. Marra, and A. Caserta (2001). Edge-diffracted 1-sec surface waves observed in a small-size intramountain basin (Colfiorito, central Italy), *Bull. Seismol. Soc. Am.* 91**,** no. 6, 1851–1866.

Scognamiglio, L., E. Tinti, A. Michelini, A. S. Dreger, A. Cirella, M. Cocco, S. Mazza, and A. Piatanesi (2010). Fast determination of moment tensors and rupture history: What has been learned from the 6 April 2009 L'Aquila earthquake sequence, *Seismol. Res. Lett.* 81**,** 892–906.

Scrocca, D. (2006). Thrust front segmentation induced by differential slab retreat in the Apennines (Italy), *Terra Nova* **18,** 154–161.

Smerzini, C., and M. Villani (2012). Broadband Numerical simulations in complex near-field geological configurations: The case of the 2009 M_w 6.3 L'Aquila earthquake, *Bull. Seismol. Soc. Am.* 102**,** no. 6, 2436–2451.

Spudich, P., and L. Xu (2003). Software for calculating earthquake ground motions from finite faults in vertically varying media, in *International Handbook of Earthquake and Engineering Seismology*, Int. Geophys. Ser., W. H. K. Lee, H. Kanamori, P. C. Jennings, and C. Kisslinger, Vol. 81, Academic, Amsterdam, 1633–1634, doi: 10.1016/S0074-6142(03)80293-0.

Spudich, P., M. Hellweg, and W. H. K. Lee (1996). Directional topographic site response at Tarzana observed in aftershocks of the 1994 Northridge, California, earthquake: Implications for mainshock motions, *Bull. Seismol. Soc. Am.* **86,** no. 1B, S193–S208.

Stich, D., and A. Morelli (2007). Reflection of seismic surface waves at the northern Apennines, *Earth Planet. Sci. Lett.* **259,** 149–158.

Stich, D., P. Danecek, A. Morelli, and J. Tromp (2009). Imaging lateral heterogeneity in the northern Apennines from time reversal of reflected surface waves, *Geophys. J. Int.* **177,** 543–554.

Stupazzini, M., R. Paolucci, and H. Igel (2009). Near-fault earthquake ground-motion simulation in the Grenoble valley by a high-performance spectral element code, *Bull. Seismol. Soc. Am.* **99,** no. 1, 286–301.

Tape, C., Q. Liu, A. Maggi, and J. Tromp (2010). Seismic tomography of the southern California crust based on spectral-element and adjoint methods, *Geophys. J. Int.* **180,** 433–462.

Tape, C., Q. Liu, and J. Tromp (2007). Finite-frequency tomography using adjoint methods—Methodology and examples using membrane surface waves, *Geophys. J. Int.* **168,** no. 3, 1105–1129.

Tarantola, A. (1984). Inversion of seismic reflection data in the acoustic approximation, *Geophysics* **49,** 1259–1266.

Tarrass, I., L. Giraud, and P. Thore (2011). New curvilinear scheme for elastic wave propagation in presence of curved topography, *Geophys. Prospect.* **59,** 889–906.

Tinti, E., E. Fukuyama, A. Piatanesi, and M. Cocco (2005). A kinematic source time function compatible with earthquake dynamics, *Bull. Seismol. Soc. Am.* **95,** 1211–1223.

Trasatti, E., C. Kyriakopoulos, and M. Chini (2011). Finite element inversion of DInSAR data from the M_w 6.3 L'Aquila earthquake, 2009 (Italy), *Geophys. Res. Lett.* **38,** L08306, doi: 10.1029/2011GL046714.

Tromp, J., D. Komatitsch, and Q. Liu (2008). Spectral-element and adjoint methods in seismology, *Comm. Comput. Phys.* **3,** no. 1, 1–32.

Tromp, J., C. Tape, and Q. Liu (2005). Seismic tomography, adjoint methods, time reversal and banana-doughnut kernels, *Geophys. J. Int.* **160,** no. 1, 195–216.

Virieux, J. (1986). *P-SV* wave propagation in heterogeneous media: Velocity-stress finite-difference method, *Geophysics* **51,** 889–901.

Volpe, M., A. Piersanti, and D. Melini (2012). Complex 3D Finite Element modeling of the April 6th 2009 L'Aquila Earthquake by inverse analysis of static deformation, *Geophys. J. Int.* **188,** 1339–1358.

Wald, D. J., V. Quitoriano, T. H. Heaton, and H. Kanamori (1999). Relationships between peak ground acceleration, peak ground velocity, and Modified Mercalli intensity in California, *Earthq. Spectra* **15,** 557–564.

Zaccarelli, L., N. M. Shapiro, L. Faenza, G. Soldati, and A. Michelini (2011). Variations of crustal elastic properties during the 2009 L'Aquila earthquake inferred from cross-correlations of ambient seismic noise, *Geophys. Res. Lett.* **38,** L24304, doi: 10.1029/2011GL049750.

Zhu, H., E. Bozdağ, D. Peter, and J. Tromp (2012a). Structure of the european upper mantle revealed by adjoint tomography, *Nat. Geosci.* **5,** 493–498.

Zhu, H., E. Bozdağ, D. Peter, and J. Tromp (2012b). Seismic wavespeed images across the iapetus and tornquist suture zones, *Geophys. Res. Lett.* **39,** no. 18, L18304, doi: 10.1029/2012GL053053.

Istituto Nazionale di Geofisica e Vulcanologia
Via di Vigna Murata 605
00143 Rome, Italy
federica.magnoni@ingv.it
(F.M., E.C., A.M., A.P.)

LMA, CNRS UPR 7051
Aix-Marseille University
Centrale Marseille
13402 Marseille Cedex 20, France
(D.K.)

Institute of Geophysics
ETH Zurich
NO H1.2, Sonneggstrasse 5
8092 Zurich, Switzerland
(D.P.)

Department of Geosciences and Program in Applied & Computational Mathematics
Princeton University
Princeton, New Jersey 08544
(J.T.)

Manuscript received 2 May 2013;
Published Online 31 December 2013